

# 1 Target-agnostic discovery of Rett Syndrome therapeutics by coupling 2 computational network analysis and CRISPR-enabled *in vivo* disease modeling

3

4 Novak, R.<sup>1,†,\*</sup>, Lin, T.<sup>1,\*</sup>, Kaushal, S.<sup>1</sup>, Sperry, M.<sup>1</sup>, Vigneault, F.<sup>1,†</sup>, Gardner, E.<sup>1,†</sup>, Loomba, S.<sup>1</sup>,  
5 Shcherbina, K.<sup>1</sup>, Keshari, V.<sup>1</sup>, Dinis, A.<sup>1</sup>, Vasan, A.<sup>1</sup>, Chandrasekhar, V.<sup>1</sup>, Takeda, T.<sup>1</sup>, Turner,  
6 J.R.<sup>2</sup>, Levin, M.<sup>1,3</sup>, Ingber, D.E.<sup>1,4,5,#</sup>

7

<sup>8</sup> <sup>1</sup>Wyss Institute for Biologically Inspired Engineering, Harvard University, Boston, MA, USA

9   <sup>2</sup>Laboratory of Mucosal Barrier Pathobiology, Department of Pathology, Brigham and Women's  
10 Hospital and Harvard Medical School, Boston, MA, USA

11 <sup>3</sup> Allen Discovery Center at Tufts University, Medford, MA, USA

12   <sup>4</sup> Harvard John A. Paulson School of Engineering and Applied Sciences, Harvard University,  
13   Cambridge, MA, USA

14     <sup>5</sup>Vascular Biology Program and Department of Surgery, Boston Children's Hospital and Harvard  
15     Medical School, Boston, MA, USA

16 <sup>†</sup>Present address: Unravel Biosciences, Inc., Boston, MA, USA

17 \* Contributed equally to this manuscript

18

19 # Corresponding author: Donald E. Ingber, MD, PhD

20 Wyss Institute at Harvard University

21 CLSB5, 3 Blackfan Circle

22 Boston, MA, 02115 USA

23 E-mail: don.ingber@wyss.harvard.edu

24

25      **ABSTRACT**

26            Many neurodevelopmental genetic disorders, such as Rett syndrome, are caused  
27            by a single gene mutation but trigger changes in expression and regulation of numerous  
28            other genes. This severely impair functions of multiple organs and organ systems  
29            beyond the central nervous system (CNS), adding to the challenge of developing broadly  
30            effective treatments based on a single drug target. This challenge is further complicated  
31            by the lack of sufficiently broad and biologically relevant drug screens, and the inherent  
32            complexity in identifying clinically relevant targets responsible for diverse phenotypes.

33            Here, we combined human gene regulatory network-based computational drug prediction  
34            with *in vivo* screening in a population-level diversity, CRISPR-edited, *Xenopus laevis*  
35            tadpole model of Rett syndrome to carry out target-agnostic drug discovery, which  
36            rapidly led to the identification of the FDA-approved drug vorinostat as a potential  
37            repurposing candidate. Vorinostat broadly improved both CNS and non-CNS (e.g.,  
38            gastrointestinal, respiratory, inflammatory) abnormalities in a pre-clinical mouse model  
39            of Rett syndrome. This is the first Rett syndrome treatment to demonstrate pre-clinical  
40            efficacy across multiple organ systems when dosed after the onset of symptoms, and  
41            network analysis revealed a putative therapeutic mechanism for its cross-organ  
42            normalizing effects based on its impact on acetylation metabolism and post-translational  
43            modifications of microtubules. Although traditionally considered an inhibitor of histone  
44            deacetylases (HDAC), vorinostat unexpectedly restored protein acetylation across both  
45            hypo- and hyperacetylated tissues, suggesting non-HDAC-mediated therapeutic  
46            mechanisms supported by proteomic analysis.

47

48 **INTRODUCTION**

49 Rett Syndrome (Rett) is a neurodevelopmental disorder that is also known to clinically  
50 impact multiple organs and systems in the body. It is primarily caused by mutations of the gene  
51 encoding methyl-CpG binding protein (MeCP2), a ubiquitous nuclear protein that acts as a  
52 transcriptional repressor and activator affecting hundreds of genes across the genome  
53 (Chahrour and Zoghbi, 2007). Rett is characterized by a high degree of cellular heterogeneity,  
54 with a mixture of wild type and MeCP2 mutant cells within the tissues of the same individual  
55 (Renthal et al., 2018) that leads to subtle but widespread gene misregulation (Gabel et al.,  
56 2015). Clinical criteria and research on Rett have primarily focused on neuromotor, social, and  
57 cognitive impairments and other CNS symptoms (e.g., seizures, repetitive purposeless  
58 movements, regression, microcephaly, loss of speech, autistic features)(Colvin et al., 2003; Kerr  
59 et al., 2001). However, these patients also commonly exhibit multiple clinical symptoms outside  
60 of the CNS, including respiratory dysfunction, gastrointestinal issues, systemic inflammation,  
61 disrupted metabolism, circadian rhythm and sleep disturbances, abnormal bone density, kidney  
62 function, nociception derangement, which are a major source of morbidity that contribute to a  
63 shortened lifespan (Hagberg, 2002; Vashi and Justice, 2019). It is important to note that  
64 although Rett is considered a neurodevelopmental disorder and therapeutics development has  
65 focused on CNS-related endpoints, these system-wide symptoms are often the most disturbing  
66 to patients and families, and thus there is a need to ameliorate symptoms of this disease across  
67 the entire body.

68 Monogenic diseases are theoretically amenable to gene therapy treatment, and Rett has  
69 been shown to be reversible in a mouse model of X chromosome reactivation (Przanowski et  
70 al., 2018) and post-natal expression of MeCP2 (Giacometti et al., 2007; Guy et al., 2007).  
71 However, even if current challenges around delivery efficacy and safety could be overcome,  
72 Rett and other X-linked disorders require gene dosage compensation to avoid toxicity due to

73 overexpression of the corrected gene since even a modest 20% deviation of MeCP2 expression  
74 levels can lead to Rett symptoms (Collins et al., 2004; Luikenhuis et al., 2004). Therefore,  
75 pharmaceutical treatments for Rett and other neurodevelopmental disorders are still needed.  
76 Trofinetide, a synthetic IGF-1 C-terminal tripeptide activating BDNF expression, has shown  
77 initial promise in phase II clinical trials and it progressed to phase III trials but demonstrated only  
78 moderate efficacy (Glaze et al., 2017). Sarizotan, a 5-HT1A and D2 receptor agonist with  
79 promising efficacy in mouse models of Rett (Abdala et al., 2014), was recently terminated after  
80 clinical trial results failed to demonstrate efficacy (NCT02790034). Esketamine, an N-methyl D-  
81 aspartate receptor (NMDAR) agonist, is also being evaluated in the clinic (NCT03633058) due  
82 to its reduction of neuroexcitatory glutamate. But these and other therapeutic paths for Rett  
83 pursued thus far target only a subset of patients' CNS symptoms and have not shown any  
84 effects on extra-CNS morbidity.

85 Here we present an integrated approach combining a novel gene expression network  
86 computational model to predict existing drugs and screening in an in vivo phenotypically diverse  
87 model of Rett syndrome generated in *Xenopus* tadpoles to assess whole-body efficacy. Our  
88 results led to the identification of vorinostat, which showed significant efficacy in a mouse Rett  
89 syndrome model even when initiating treatment after the onset of symptoms, demonstrating the  
90 utility of the target-agnostic platform for predicting drugs to restore multi-organ system function  
91 in Rett syndrome and potentially other complex diseases.

92

## 93 **METHODS**

### 94 ***X. laevis* care and rapid generation of Rett syndrome tadpole models**

95 *Xenopus* embryos and tadpoles were housed at 18°C with a 12/12 h light/dark cycle in  
96 0.1X Marc's Modified Ringer's (MMR) medium. Tadpoles were fed 3x/week with sera Micron

97 Nature fry food. All animal experiments and procedures were reviewed and approved by the  
98 Harvard Medical School (HMS) Institutional Animal Care and Use Committee regulations.  
99 Xenbase (Nenni et al., 2019) ([www.xenbase.org](http://www.xenbase.org)) was used to search for MeCP2 homolog in  
100 *Xenopus laevis* (*Xenopus laevis* J-strain 9.2 version). MeCP2.L (XB-GENE-17346751),  
101 MeCP2.S (XB-GENE-494744), found on Chromosome 8L and 8S, show 75% and 70%  
102 sequence identity with human MeCP2, respectively. An important biological distinction is that  
103 while human MeCP2 is found on the X chromosome, Chromosome 8 is not part of the sex  
104 determination alleles of homomorphic chromosome pairs in *X. laevis*. Cas9 target sites were  
105 selected using CHOPCHOP (Labun et al., 2016) on the *X. laevis* J-strain 9.2 version, which  
106 facilitated the selection of guide RNA with no predicted off-targets. We used the default settings  
107 to generate a list of target sequences. We selected 4 targets from this list for each of the L and  
108 S forms. This selection was based primarily on the ranking provided by CHOPCHOP and as a  
109 function of their location on MeCP2 to target exons coding for the methyl-CpG-binding domain  
110 (MBD, exons 2 and 3) and Transcriptional repression domain (TRD, exon 3). The 8 sgRNA  
111 sequences are presented in **Supplementary Table 9** and were synthesized as modified sgRNA  
112 by Synthego Inc.

113 The sgRNA were resuspended to 100 µM in 0.1X Tris EDTA (pH 8.0). Then, an  
114 equimolar sgRNA mix was made using 2 µl of each sgRNA, for a total of 16 µl. The Cas9 RNP  
115 complex was formed by mixing 75 pmol of the sgRNA mix with 75 pmol of Cas9 in annealing  
116 buffer (5 mM HEPES, 50 mM KCl, pH 7.5), for a total volume of 100 µL, then incubated at 37°C  
117 for 10 minutes. The RNP was kept frozen at -20°C until the day of the injection. To generate  
118 MeCP2 knockdown models of Rett syndrome, *Xenopus* embryos were fertilized and maintained  
119 at 14°C until the 4-cell stage. Each cell was injected with ~2 nL RNP per injection resulting in a  
120 final amount of 1.5 fmol of RNP per injection per cell, and we did not see any adverse effect  
121 when controlling for Cas9 or sgRNA at that amount. Note that the 1.5 fmol of ribonucleoprotein

122 (RNP) used per injection is two to five time less than what has been commonly used in  
123 previously published studies for *Xenopus* (Aslan et al., 2017) as we found that higher amounts  
124 of sgRNA had adverse effects (not shown). Following injections, embryos were kept in 0.1X  
125 MMR at 18°C as described above, for the 18 days duration of the experiment.

126 **PCR and fragment analysis to validate MeCP2 gene disruption**

127 MeCP2 editing efficiency was measured using Indel Detection by Amplicon Analysis  
128 (Yang et al., 2015), which leverages PCR using a pair of primers and universal fluorescein  
129 labeled oligo (**Supplementary Table 10**). The primers were synthesized by IDT. The amplicons  
130 were purified (Zymo Research) and submitted for fragment analysis on an ABI 3730XL  
131 (performed by Genewiz) following the IDAA method described previously. ProfileIT IDAA  
132 analysis software (COBO Technologies) was used to analyze the fragments and visualize the  
133 distribution of indels and visualize out-of-frame indels (Lonowski et al., 2017). IDAA is a robust  
134 method with 1-bp resolution suited for the analysis of a tetraploid genome without the need for a  
135 deep sequencing approach.

136 We analyzed the indels of 3 target sites on MeCP2.S of 14 tadpoles presenting with  
137 seizures and 3 non-edited tadpoles. Using a window of +/- 100 bp from the target site, we  
138 observed varied editing efficiencies depending on the target site. The likely out-of-frame indels  
139 ratio averaged 47% for XI-mecp2s-g01 on exon 3, with the lowest being 12% for a given tadpole  
140 and highest being 95%, 48% for XI-mecp2s-g02 on exon 2 (min/max 20-84%), and ~82% for XI-  
141 mecp2s-g04 on exon 2 (min/max 7-91%). Overall, 98% of indels where between 1 to 30 bp, and  
142 84% were deletions.

143 **Microarray analysis**

144 Tadpoles were sacrificed at stage 50 of development and lysed using a QIAGEN  
145 TissueLyser II bead mill (30 Hz, 2 x 30 sec) in a 2 mL tube with a 2.4 mm steel beads (Omni)

146 and 1 mL phosphate buffered saline buffer at 4°C. 250 mL of lysate was used for RNA  
147 extraction using a QIAGEN RNeasy mini kit. RNA samples were DNase treated. *Xenopus laevis*  
148 Genome 2.0 Array (Affymetrix) microarrays were processed by Advanced Biomedical  
149 Laboratories (Cinnaminson, NJ). RNA samples were processed using a Nugen Ovation PICO  
150 WTA System V2 kit. The resulting cDNAs were purified using a Qiagen MinElute PCR  
151 Purification Kit following the modifications outlined in the Nugen protocol. The cDNAs were  
152 fragmented and labeled using a Nugen Encore Biotin Module. Hybridization solutions were  
153 prepared by combining the fragmented, biotin-labeled cDNAs with hybridization cocktail  
154 (Affymetrix Hybridization, Wash, and Stain Kit). The mixtures were incubated in a thermal cycler  
155 at 99 °C for 2 min followed by 45 °C for 5 min. then loaded on *Xenopus laevis* Genome 2.0  
156 arrays and incubated for 16-20 hours at 45 °C and 60 rpm in an Affymetrix Hybridization Oven  
157 645. Following hybridization, arrays were washed and stained on Affymetrix Fluidics Station  
158 450s using the Affymetrix FS450\_0001 protocol with the stains and buffers supplied in the  
159 Affymetrix Hybridization, Wash, and Stain Kit. The stained arrays were scanned at 532 nm  
160 using an Affymetrix GeneChip Scanner 3000.

161 **Transcriptomics Data Processing**

162 Microarray datasets were RMA normalized. RNAseq gene counts were normalized using  
163 size factors similar to the normalization performed by the R package DESeq. Genes missing  
164 values were removed and duplicates were combined by taking the maximum across counts.  
165 Gene expression heatmaps and hierarchical clustering plots were generated for all groups using  
166 the R package limma (version 3.42.2) and Python package seaborn (version 0.9.0). Volcano  
167 plots were generated using the Python package bioinfokit (version 0.7).

168 **nemoCAD Drug Prediction Algorithm**

169        In the present study, we developed the nemoCAD computational tool to predict drugs  
170      that would shift MeCP2-edited tadpoles to a control tadpole state based on transcriptome state  
171      for each condition. nemoCAD utilizes pre-computed interaction probabilities of drug-gene and  
172      gene-gene interactions and differential gene expression signatures of a disease state and  
173      appropriate control to identify compounds capable of changing a transcriptional signature  
174      indicative of one biological state to another state of interest (e.g., reverting a disease state to a  
175      healthy state).

176        The repurposing algorithm is first used to identify transcriptome-wide differential  
177      expression profiles between two biological states in the input transcriptomic dataset  
178      (experimental or published) and to define the target normalization signature, i.e., the subset of  
179      genes whose expression levels need to be reversed in order to revert one state to the other  
180      (e.g., normalize the diseased state). Pairwise analysis, that implicitly assumes genes are  
181      expressed independently of one another, is carried out based on the comparison between gene  
182      expression profiles of >19,800 compounds found in the LINCS database release v1  
183      (Subramanian et al., 2017) and the target normalization signature. Multiple correlation statistics  
184      (e.g., Pearson correlation, cross-entropy) across all differentially expressed genes are  
185      calculated and a combination score (e.g., Pearson correlation divided by the cross-entropy) is  
186      computed.

187        Putative predictions that incorporate gene-gene dependencies are then generated  
188      separately based on Bayesian network analysis on a regulatory and drug-gene interaction  
189      network architecture defined using publicly available databases of gene-gene interactions based  
190      on single gene knockout datasets in human cells (KEGG, TRRUST) and reference  
191      transcriptional signatures of drugs (LINCS, CTD), as described below. By combining a directed  
192      unweighted network structure with interaction probabilities for the connecting network edges,  
193      the constructed network is a weighted directed graph consisting of all possible paths that

194 connect at least 2 genes of interest from the relevant genes within the target transcriptomic  
195 normalization set and the drugs; it therefore encodes the entire region of influence of a given list  
196 of genes and the drugs that can reverse their gene expression profiles in the desired manner.  
197 This network is then used as input for a message-passing algorithm (e.g. loopy belief  
198 propagation algorithm (Forbes, 2021; Pearl, 1982)) in which the marginal probability  
199 distributions of drugs being “on” given the expression state of every gene are computed using  
200 the joint probability distribution encoded in the . This network-based approach leads to a ranking  
201 of all the drugs based on the probability of them inducing the desired transcriptomic signature  
202 across all genes in the network, which is separate from the initial ranking based on correlation  
203 analysis described above. This method has the advantage of incorporating gene-gene  
204 dependencies, but its success relies on the quality of network structures curated in the source  
205 databases.

206         Ultimately, drugs are prioritized that have both high correlation with the desired  
207 transcriptional signature change, representing desired drug-gene interactions, and high  
208 probabilities of being able to reverse the diseased state predicted by the Bayesian network  
209 analysis, representing gene network-level drug effects that can counter network-level disease  
210 processes. nemoCAD also enables visualization of the architecture of the network and  
211 subnetworks, and thus provides insight into potential molecular targets that can be verified using  
212 additional experiments. nemoCAD also can be used to optimize treatment regiments by  
213 iteratively inputting animal omics data following drug treatment to further tune drug predictions  
214 and develop drug combinations that might synergize in unpredictable ways. The approach  
215 underlying nemoCAD avoids the needs for *a priori* target or pathway inputs and, in fact, enables  
216 their discovery.

217

218

219 **Transcriptomics Gene Network Construction**

220 Gene regulatory networks were inferred from gene expression data using the  
221 Bioconductor package GEne Network Inference with Ensemble of trees (GENIE3) release 3.12  
222 in RStudio (R version 3.6.2)(Huynh-Thu et al., 2010). GENIE3 infers a weighted, directed gene  
223 regulatory network from expression data by decomposing the prediction of a network between  $k$   
224 genes into  $k$  different regression problems. For each individual regression analysis, the  
225 expression pattern of one of the genes (target gene) is predicted from the expression patterns of  
226 all the other genes (regulator genes) using ensembles of regression trees. GENIE3 produces an  
227 adjacency matrix representation of the network with  $k$  nodes in which each node represents a  
228 gene, and an edge directed from one gene  $i$  to another gene  $j$  indicates that gene  $i$  regulates the  
229 expression of gene  $j$ . Based on known mechanisms involved in Rett Syndrome  
230 (**Supplementary Table 1**), a subset of genes was selected as candidate regulators: BDNF,  
231 FCRL2, FMR1, MeCP2, NTRK2, PER1, PER2, and PUM1. These potential regulators were  
232 calculated over all available target genes in the transcriptomics datasets (10,934 genes) for  
233 MeCP2 knock down and cas9-injected control samples. Digraph objects were constructed from  
234 adjacency matrices and visualized in Matlab R2020a (Mathworks; Natick, MA) for each of the  
235 MeCP2 knock down and control groups. The strongest regulator gene-target gene relationships  
236 were highlighted by filtering each network at a consistent edge weight ( $e_w$ ) threshold ( $e_w = 0.3$ )  
237 prior to plotting.

238 **Cross-Species Transcriptomics Analysis**

239 Gene networks involved in Rett Syndrome in human patients and MeCP2 knock down in  
240 laboratory animal models were compared using previously acquired transcriptomics datasets  
241 (**Supplementary Table 2**). Transcriptomics datasets were processed using the same methods  
242 described for *Xenopus* transcriptomics and normalized using a series of transformations. Since  
243 RNA-seq data typically have a wider dynamic range than microarray datasets, RNA-seq and

244 microarray data was transformed into a common space (Sekhon et al., 2013). RNA-seq  
245 datasets were transformed using a hyperbolic sine function and the  $\log_2$  transformation was  
246 applied to microarray data (Sekhon et al., 2013). Subsequently, a variance stabilizing  
247 transformation was applied to remove potential mean-variance relationships in each dataset  
248 (Russo et al., 2018). Common genes expressed and measured between datasets (926 genes)  
249 were considered for further analysis. Dimensional reduction was performed using Principle  
250 Component Analysis (PCA) and visualized using Uniform Manifold Approximation and  
251 Projection (UMAP) in Python with the help of sklearn and UMAP packages.

252 Commonalities in gene expression values across species were analyzed by plotting  
253 heatmaps of differential gene expression using the Python packages seaborn and matplotlib. All  
254 datasets were normalized as described above and log fold change for each gene was  
255 calculated by combining samples of a condition using geometric mean. Log fold changes for all  
256 species were combined and the genes (96 genes) with variance greater than the mean variance  
257 (in fold changes) were used to construct the heatmaps.

258 Transcriptomics gene networks were constructed using GENIE3 and the same methods  
259 previously described. To investigate potential changes across the entire gene network, regulator  
260 genes were *not* down selected. Adjacency matrices were visualized for each network and the  
261 distribution of edge weights in the network was assessed by histogram and boxplots in Matlab.  
262 Digraph objects were constructed from adjacency matrices and visualized in Matlab for the  
263 strongest connections in each network ( $e_w > 99.99\%$  for each network). Resultant networks  
264 were combined across all datasets for each species and plotted with different colors designating  
265 each dataset. A cross-species network that includes the strongest network connections across  
266 all datasets was formed by combining each species-specific dataset and plotted with different  
267 colors designating each species. To identify the strongest regulator and target gene nodes in  
268 the resultant cross-species network, the in-degree and out-degree were calculated in Matlab.

269 The in-degree is defined as the number of edges with that node as the target and out-degree of  
270 a node is equal to the number of edges with that node as the source.

271 **Drug screening**

272 Drugs for tadpole screening were purchased from Sigma-Aldrich (St. Louis , MO, USA)  
273 or MedChem Express (Monmouth Junction, NJ, USA) and dissolved in DMSO to a stock  
274 concentration of 100-1,000  $\mu$ M, depending on the solubility. For screens, compounds were  
275 diluted to their final concentrations with a 0.1% DMSO concentration. Media with dosed drug  
276 were made fresh and exchanged every two days following feeding. Dosing began at stage 45  
277 and lasted for 7 days, after which standard 0.1X MMR was used to evaluate drug washout  
278 effects. Free-swimming tadpoles were imaged in 60 mm dishes using a SONY Alpha a6100  
279 camera with 16mm objective against an illuminated background. Tadpole behavior was scored  
280 manually by noting the most severe seizure-related phenotype described by Hewapathirane et  
281 al. (Hewapathirane et al., 2008) within a 20 min period.

282 Vorinostat and trofinetide for mouse studies were purchased from MedChem Express  
283 (Monmouth Junction, NJ, USA). For intraperitoneal injection, trofinetide was solubilized in  
284 DMSO, and vorinostat was solubilized in a method previously published(Basu et al., 2019;  
285 Hockly et al., 2003). 2-hydroxypropyl- $\beta$ -cyclodextrin powder (HP $\beta$ CD) was purchased from  
286 Acros Organics (ThermoFisher, Waltham, MA, USA). Vorinostat was dissolved in 100 mM  
287 HP $\beta$ CD by boiling for 5 minutes. Mice were dosed intraperitoneally at 100mg/kg with Trofinetide  
288 and 50 mg/kg with vorinostat. For oral dosing, commercial instructions were followed to add  
289 solubilized vorinostat (100 mg/kg) to Medigel (purchased from ClearH20, Westbrook, ME, USA).

290 **X. laevis Tissue Processing**

291 After stage 46 tadpoles were euthanized with 20x Tricaine, tadpoles were washed three  
292 times with PBS (-/-) and fixed in 4% Paraformaldehyde in PBS + Mg + EGTA (MEMFA) (Alfa

293 Aesar, Tewksbury, MA, USA) for 2 hours at RT. For sections, *Xenopus* tadpoles were  
294 cryoprotected by sequential incubation of 10%, 20% and 30% sucrose in 1x PBS(-/-), only  
295 transferring to the subsequent concentration when the samples sunk to the bottom of the  
296 scintillation vial. Cryoprotected tadpoles were embedded in 5% agarose and were stored in -  
297 80°C. For GI staining, the gastrointestinal tract was microdissected with a stereoscope before  
298 embedding. Embedding tissue were sectioned coronally at 20 µm thickness on a Cryostat  
299 (Leica, CM3050 S, Wetzlar, Germany) and mounted on superfrost plus slides (Thermo Fisher,  
300 Waltham, MA, USA). Slides were dehydrated for 30 minutes at 20°C, before storing at -80°C.  
301 For whole mount preparation, tadpoles were processed in a method previously published  
302 (Willsey, 2021).

303 ***In situ* hybridization**

304 Following *X. laevis* tissue processing of cryosections, sample pretreatment, RNAscope  
305 Target Retrieval and the RNAscope Assay was conducted by the HMS Neurobiology Imaging  
306 Facility following manufacturer's instructions. XI.MeCP2 was custom designed by Advanced Cell  
307 Diagnostics. Rpl8 was used as a positive control (XI-LOC108706872-C3, Cat No. 516501-C3,  
308 Advanced Cell Diagnostics, Hayward, CA) and DapB as a negative control (Cat No. 320758,  
309 Advanced Cell Diagnostics, Hayward, CA).

310 **Immunohistochemistry of *Xenopus laevis* sections and whole mounts**

311 Following tissue processing, cryosections were blocked for 2 hours at room temperature  
312 and subsequently incubated with primary antibodies overnight at 4°C, including mouse anti-  
313 alpha acetylated tubulin (1:1000 dilution, Sigma Aldrich, Burlington, MA USA), mouse anti-beta-  
314 tubulin (1:1000 dilution, E7, Developmental Studies Hybridoma Bank, Iowa City, Iowa, USA),  
315 anti-MeCP2 (1:1000 dilution, Invitrogen, Waltham, MA USA), Hoechst (1:1000 dilution,

316 ThermoFisher, Waltham, MA, USA), negative controls anti-mouse IgG (1:1000 dilution,  
317 Invitrogen, Waltham, MA, USA), and anti-rabbit (1:1000 dilution, Invitrogen, Waltham, MA USA),  
318 as well as FITC-conjugated isolectin B<sub>4</sub> (1:1000 dilution, Thermo Fisher, Waltham, MA, USA).  
319 Slides were washed twice with TRIS-buffered saline, with 1% Tween-20 (TBT) for 5 minutes  
320 each and incubated in the dark with their corresponding secondary antibody: Goat anti-rabbit  
321 Alexa 647 (1:1000 dilution, Abcam, Waltham, MA, USA) and Goat anti-mouse Alexa 594  
322 (1:1000 dilution, Abcam, Waltham, MA, USA) for 1 hour at room temperature. Slides were  
323 washed three times with TBT for 5 minutes each on an orbital shaker and mounted in ProLong  
324 Gold Antifade Mountant (ThermoFisher, Waltham, MA, USA) with a #1 coverslip and sealed.  
325 Slides were stored in the dark at 4°C before image acquisition. Z-stacks were acquired at 1 μm  
326 to visualize brain and gastrointestinal sections.

327 *X. laevis* embryos were processed for whole mount immunofluorescence as described  
328 (Willsey, 2021). Fixed tadpoles were quenched for 1 hour in a lightbox in 5% formamide and 4%  
329 hydrogen peroxide in PBS, permeabilized for 1 hour in PBS with 0.1% Triton X-100 (PBT) and  
330 blocked for 1 hour in 10% CAS-Block in PBT (Life Technologies, Carlsbad, CA, USA). Primary  
331 antibodies were incubated overnight at 4°C, including mouse anti-alpha acetylated tubulin  
332 (1:700 dilution Sigma Aldrich, Burlington, MA USA), mouse anti-beta-tubulin (1:100 dilution, E7,  
333 Developmental Studies Hybridoma Bank, Iowa City, Iowa, USA)), Hoechst (1:100 dilution,  
334 ThermoFisher, Waltham, MA, USA) and anti-mouse IgG (1:100 dilution). Slides were washed in  
335 PBT, blocked in 10% CAS-Block for 30 minutes, and incubated with the corresponding  
336 secondary antibody for 2 hours at room temperature including Goat anti-mouse Alexa 546  
337 (1:100 dilution, Thermo Fisher, Waltham, MA, USA) and Goat anti-rabbit 633 (1:100 dilution,  
338 ThermoFisher, Waltham, MA, USA). Tadpoles are washed with PBT for 1 hour and then  
339 washed in PBS for another hour before mounting in Vectashield (Vector Laboratories,

340 Burlingame, CA, USA). Z-stacks were acquired at 1 $\mu$ m for visualizing epidermal MCC's and  
341 3 $\mu$ m for visualizing entire brain regions.

342 **Drug target discovery in *X. laevis* using thermal proteome profiling**

343 *Sample preparation*

344 While we largely followed the protein integral solubility alteration (PISA) thermal  
345 proteome profiling protocol (Gaetani et al., 2019), we adapted the mammalian cell- and tissue-  
346 specific parameters to tadpoles by optimizing the method to tadpoles by reducing thermal  
347 treatment temperatures to account for the lower normal temperature range of *X. laevis*.

348 Unmodified *X. laevis* tadpoles (stage 47-50) were exposed to 25  $\mu$ M vorinostat or 0.1  $\mu$ M  
349 ivermectin for 2 h while freely swimming in 0.1x MMR medium. Following euthanasia using  
350 Tricaine, animals were washed with fresh MMR, cut into thirds (head, abdomen containing all  
351 visceral organs, and tail), and placed into individual Eppendorf tubes covered with MMR  
352 containing the same drug and concentration and incubated for 3 min at one of 9 temperatures  
353 spanning 30-60°C. 30°C was selected as the control temperature, where no appreciable thermal  
354 denaturation should take place, based on the maximum tolerable temperature for *X. laevis*  
355 (Ruthsatz et al., 2018). Following aspiration of remaining liquid, samples were flash frozen in  
356 liquid nitrogen.

357 Samples were further processed and analyzed by Phenoswitch Bioscience, Inc.  
358 (Sherbrooke, Québec, Canada). Thermally-treated samples were lysed in 100  $\mu$ L PBS with  
359 0.4% NP-40 with 4 cycles of freeze/thaw. Insoluble material was cleared by centrifugation (10  
360 min, 10,000 G, 4°C). 11 $\mu$ L of supernatant for each of the 9 temperatures were then pooled in  
361 one tube and samples were centrifuged again at 13,000 RPM for 75 minutes, at 4°C to pellet  
362 precipitated proteins. 80  $\mu$ L of the supernatant were reduced with 10 mM DTT for 15 min at  
363 65°C and alkylated with 15 mM IAA and 30 min at room temperature in the dark. Proteins were

364 precipitated with 8 volumes of ice-cold acetone and 1 volume of ice cold methanol overnight.  
365 Protein pellets were washed 3 times with 250 µl of ice-cold methanol and resuspended in 100  
366 µL digestion buffer. Digestion was carried for 4 hours in 50 mM Tris ph 8 + 0.75 mM Urea + 1µg  
367 trypsin/LysC at 37°C with agitation. Another 1 µg of trypsin/LysC was added, and digestion was  
368 continued overnight. Peptides were purified by reversed phase SPE and analyzed by LC-  
369 MS/MS.

370 *Mass spectrometry*

371 Acquisition was performed with a TripleTOF 6600 (Sciex, Foster City, CA, USA)  
372 equipped with an electrospray interface with a 25 µm iD capillary and coupled to a Micro LC200  
373 (Eksigent, Redwood City, CA, USA). Analyst TF 1.8 software was used to control the  
374 instrument. Acquisition was performed in data independent acquisition (DIA or SWATH) using  
375 gas phase fractionation (GPF1 from 350 m/z to 800 m/z and GPF2 from 800 m/z to 1250 m/z).  
376 The source voltage was set to 5.5 kV and maintained at 325°C, curtain gas was set at 45 psi,  
377 gas one at 25 psi and gas two at 25 psi. Separation was performed on a reversed phase  
378 Kinetex XB column 0.3 µm i.d., 2.6 µm particles, 150mm long (Phenomenex) which was  
379 maintained at 60°C. Samples were injected by loop overfilling into a 5 µL loop. For the 60  
380 minutes LC gradient, the mobile phase consisted of the following solvent A (0.2% v/v formic acid  
381 and 3% DMSO v/v in water) and solvent B (0.2% v/v formic acid and 3% DMSO in EtOH) at a  
382 flow rate of 3 µL/min. Both GPF files were analyzed on a previously-generated 3D ion library  
383 using the SWATH 2.0 microapp from Peakview (Sciex, Foster City, CA, USA). Each GPF file  
384 was analyzed using 10 peptides per protein, 4 MS/MS transition per peptide, 12.5 min RT  
385 window and 25 ppm XIC width. The reported quantification for a protein is the sum of all the  
386 correctly integrated peptides (FDR<0.05) in both GPF files.

387 **Mouse care**

388            Experiments were performed with MeCP2-null (*MeCP2<sup>-/-</sup>*) (strain 003890) and age-  
389 matched WT male littermates (*MeCP2<sup>+/+/-</sup>*), purchased from Jackson Laboratories (Bar Harbor,  
390 ME). All mice were housed in ventilated racks under specific-pathogen-free conditions at a room  
391 temperature in a 12/12 h light/dark cycle with food and water ad libitum. All animal experiments  
392 and procedures were reviewed and approved by the Harvard Medical School (HMS) Institutional  
393 Animal Care and Use Committee regulations. Every effort was made to minimize their suffering.  
394 Mice were assessed for disease severity and endpoint criteria on a daily basis by weighing and  
395 using the phenotypic scoring method developed by the Bird laboratory (Guy et al., 2007;  
396 Szczesna et al., 2014), which includes assessing mobility, gait, breathing, tremor, and general  
397 condition. Endpoint was determined by 20% body mass loss or a score of 2 in criteria D, E, or  
398 F. Dosing and Behavioral procedures began when mice reached 4 weeks of age.

399            **Behavioral Testing**

400            *Elevated Plus Maze (EPM)*

401            The elevated plus maze (EPM) consisted of two open and two closed (34 cm long and 5  
402 cm wide) arms extended out from a central platform 50 cm above the floor. The test was carried  
403 out in dim ambient lighting. The room of the experiment and its spatial cues were kept  
404 consistent and minimal. Mice were habituated in the test room for 30 minutes before the start of  
405 the test. Mice were placed near the center compartment of the maze, facing an open arm, and  
406 allowed to explore the apparatus for 5 minutes. After each test, the maze was cleaned  
407 thoroughly with 70% ethanol and left to dry before the start of the next test. A computer-assisted  
408 video-tracking system (EthoVision XT 14, Noldus, Leesburg, VA) was used to record the  
409 number of open and closed arm entries as well as the total time spent in open, closed, and  
410 center compartments. An increase in the percent time spent or entries into the open arms was  
411 used as a surrogate measure of anxiolytic-like behavior (Carobrez and Bertoglio, 2005).

412     *Spatial Novelty Y-Maze (Y-maze)*

413         The spatial novelty y-maze consisted of a Y-shaped maze with three arms at a 120° from  
414         each other as well as a removable blockade used to prevent access to one of the arms during the  
415         Habituation phase. The test was carried out in dim ambient lighting. The room of the experiment  
416         and its spatial cues were kept consistent. One of the three arms was defined as the start arm,  
417         where the mice would be placed at the start of the experiment and was kept consistent throughout  
418         the entire study. The test consisted of a three-minute Habituation phase where one of the two  
419         non-start arms was blocked off, a two-minute intertrial interval (ITI) outside of the maze and a  
420         three-minute Test phase, where the previously blocked arm was exposed to the mouse. The arm  
421         that was blocked off during the Habituation phase was randomized and noted for each mouse.

422         Mice were kept in an adjacent room to not disturb the test. The test mouse was placed in  
423         a holding cage and brought to the test room with the maze and immediately placed into the Y-  
424         maze at the designated start arm and allowed to explore the start and familiar arm trial for three  
425         minutes. At the end of the habituation phase, the mouse was placed into the holding cage for 2  
426         minutes ITI. During this time, the blockade was removed, and the maze was cleaned with an  
427         ammonia-based cleaner with a paper towel and left to dry to remove odor cues. The mice were  
428         then placed back in the start arm and left to explore the entire maze for three minutes. After the  
429         test trial, the mouse was transported back to its home cages and the maze was again wiped dry  
430         with an ammonia based cleaner. A computer-assisted video tracking system (EthoVision XT 14,  
431         Noldus, Leesburg, VA) was used to record the number of entries, time spent in each arm and as  
432         distance traveled in each arm during the Habituation and Test Phase. The percentage of time and  
433         distance spent in the novel, or previously blocked arm were used to assess spatial novelty seeking  
434         behavior (Dellu et al., 2000).

435

436 **Mouse Histology and Immunostaining**

437 Mice were euthanized with CO<sub>2</sub> inhalation, transcardially perfused with PBS (-/-) and 4%  
438 PFA, and tissues of interest were removed. Regions of the gastrointestinal tract and lung  
439 processed as was described previously(Morton and Snider, 2017; Nalle et al., 2019; Tsai et al.,  
440 2017). Paraffin blocks were sectioned into 15  $\mu$ m thickness. Mouse lung tissues were sectioned  
441 coronally and GI tissues were stained with hematoxylin and eosin (H&E) by the Beth Israel  
442 Deaconess Medical Center's IHC Core Facility. The slides were also stained for rabbit anti-  
443 acetylated  $\alpha$ -tubulin (ABclonal, ab179484, Woburn, MA, USA) mouse anti-CD-64 (R&D systems,  
444 AF3628, Minneapolis, MN, USA), chicken anti- $\beta$ III-tubulin (Biologend, 801202, San Diego, CA,  
445 USA) immunofluorescence by Beth Israel Deaconess Medical Center's IHC Core Facility.

446 Mouse brains were fixed with 4% paraformaldehyde at 4°C overnight, cryoprotected in a  
447 sucrose gradient (10%, 20% and 30%), and subsequently embedded in OCT Tissue Tek. The  
448 embedded tissues were subsequently sectioned coronally at 30 $\mu$ m and the free-floating sections  
449 were stained as previously described(Potts et al., 2020). The sections were blocked with 10%  
450 CAS Block in PBT for 1hr, stained with primary antibody (rabbit anti-iba-1, 1:1000, Wako, #019-  
451 19741; mouse anti-NeuN, 1:1000, Abcam, #ab104224; Hoechst, 1:1000, Thermo Fisher, H1399)  
452 overnight at 4°C. After three 10-minute washes in PBS (-/-) on an orbital shaker, the sections were  
453 stained in secondary antibody (anti-rabbit Alexa 647 for iba1, anti-mouse Alexa 594 for NeuN) for  
454 1 hour at room temperature. After three 10-minute washes on an orbital shaker, the sections were  
455 mounted on superfrost plus slides (ThermoFisher, Waltham, MA, USA) in ProLong Gold Antifade  
456 Mountant (ThermoFisher, Waltham, MA, USA) with a #1 coverslip and sealed. Z-stack images  
457 were acquired at 1 $\mu$ m intervals using the 63x/ glycerol.

458

459

460 **Multiplex Chemokine Assay**

461 After mouse euthanization, blood was collected by cardiac puncture using at 23G needle  
462 in ethylenediamine tetra-acetic acid (EDTA) treated tubes (Microvette 200 K3EDTA, CAT#  
463 20.1288.100, Sarstedt, Numbrecht, Germany). To avoid hemolysis, the tubes were kept at room  
464 temperature and quickly processed for plasma. Tubes were centrifuged at 2000 x g for 10  
465 minutes and the plasma was separated and stored in -80C until assayed. Chemokine levels  
466 were measured in mouse plasma using the Bio-Plex Pro Mouse Chemokine Panel 31-Plex  
467 (Cat# 12009159, Bio Rad, Hercules, CA, USA). Measurements were performed using the Bio-  
468 Plex 3D Suspension Array System (BioRad, Hercules, CA, USA), following the manufacturer's  
469 instructions.

470 **Microscopy and Image Processing**

471 H&E slides were imaged with 4x and 20x objectives with the Biotek Cytation 5.  
472 Immunofluorescent *Xenopus* whole mounts and *Xenopus* and mouse stained sections were  
473 imaged with the Leica SP5 X MP Inverted Confocal Microscope using 25x (NA 0.95) water  
474 objective and 63x (NA 1.3) Glycerol objectives. Sections were imaged in white light and diode  
475 laser scanning mode and whole mounts were imaged using multiphoton pulsed IR laser  
476 scanning. Serial scanning was used during acquisition to avoid bleed-through. Image settings  
477 were kept constant between groups, in terms of laser power, bit-depth, z-stack interval,  
478 resolution (pixels), aperture settings, and gain/offset. Images were post-processed and  
479 analyzed using ImageJ (Fiji, NIH).

480 *MCC morphological analysis*

481 2-photon images of *X. laevis* 25x and 63x MCC's were maximum projected, background  
482 subtracted, and subsequently assessed for cilia orientation and cilia length, as previously  
483 described (Chien et al., 2018).

484 *MCC Functional Assay*

485 We visualized the cilia-driven flow of fluorescent microspheres over the surface of the *xenopus*  
486 tadpole by taking times series with the Leica SP5 x MP inverted confocal. Our methods were  
487 based on previous reports (Kulkarni et al., 2018) with some modifications. Stage 45 tadpoles  
488 were placed in a 24 well  $\mu$ -Plate 14mm (ibidi, Gräfelfing, Germany), and underwent anesthesia  
489 by incubation with 1x tricaine before proceeding to image. One tadpole was placed per well for  
490 individual tracking. Fluorescent microspheres beads (Thermo Fisher, Waltham, MA) were added  
491 at a final dilution of 1:100. We chose the bead size of  $3\mu\text{m}$ , because during preliminary testing  
492 and as is reflected in the data, WT *X. laevis* tadpoles consistently was able to clear beads that  
493 were  $3\mu\text{m}$  diameter at this concentration. The Leica SP5 x MP laser scanning mode was used  
494 to visualize the fluorescent microspheres beads at an excitation of 520nm and emission of  
495 560nm with the following settings: 512x512 pixels, bidirectional scanning mode, and at a scan  
496 speed of 800-1600Hz, with the 25x (NA 0.95) water objective, and over the time course of 5  
497 minutes every 5s. Time series were acquired of in the olfactory and lateral region of the  
498 epidermis.

499 *Quantification of bead displacement*

500 The time series stacks were maximum intensity projected to visualize the overall bead flow.  
501 Intensity was measured as a function from the distance from the surface of the epidermis.

502 *Mean Intensity Quantitation*

503 To generate a ROI mask, channels acquired in one z-stack were split and the maximum  
504 intensity projection of a ‘control’ channel was taken. In the case for assessing  $\alpha\text{aT}$  expression  
505 mouse GI tract and bronchiole, the  $\beta\text{III-tubulin}$  channel was used, and for assessing MeCP2  
506 expression, the  $\alpha$  -acetylated tubulin channel was used in the image stack. Subsequently,  
507 background noise was subtracted, and auto-thresholded, whose settings were held constant

508 between groups. The ROIs generated from the control channel were used to quantify the  
509 maximum projected channel of interest, to obtain the mean intensity (integrated density per  
510 area). A minimum of 3 serial sections were analyzed per animal.

511 *Counting Ib4+ cells*

512 Confocal Z-stacks of *X. laevis* GI tract images were quantified for IB4+ cells, by taking the  
513 maximum intensity projection of the ib4+ channel. Following noise reduction, and auto-  
514 threshold, ib4+ cells were segmented and counted using the particle analysis function in the  
515 ImageJ software (NIH, Bethesda, MD).

516 *Sholl Analysis*

517 Sholl analysis was performed as previously published<sup>47</sup>. Confocal (at 1um intervals) Z-stacks  
518 were maximum intensity projected in the iba-1 channel, noise de-speckled, subsequently  
519 segmented using the auto-threshold function, and microglia were duplicated into 8-bit TIF files,  
520 in the field of view, ensuring that for each mouse at least 10 microglia were selected in the  
521 ipsilateral and contralateral region of the olfactory bulb. Using the Sholl analysis plugin in  
522 ImageJ (NIH, Bethesda, MD), traces and intersections were generated.

523 **Statistical analysis**

524 Statistical analysis of biological results was performed using Graphpad Prism 9.3. For  
525 comparison of two conditions, Student's t-test was used unless otherwise indicated. ANOVA  
526 with pairwise t-tests and Bonferroni correction or the Holm-Šídák tests was used to evaluate  
527 significance of multiple variables. P values <0.05 were considered significant (\*, p < 0.05; \*\* p <  
528 0.01; \*\*\* p < 0.001; \*\*\*\* p < 0.0001). Tadpole screens and mouse studies were conducted with  
529 5-8 animals each and repeated, except for the mouse oral dosing study.

530

531 **RESULTS**

532 **Modeling Rett syndrome genetic and phenotypic heterogeneity in *Xenopus laevis***

533 A major challenge to Rett therapeutics discovery lies in the inherent heterogeneity  
534 observed in patients stemming from gene expression variability due to the gene regulatory  
535 impact of distinct MeCP2 mutations, combined with tissue heterogeneity caused by mosaicism  
536 resulting from X chromosome inactivation. As a result, Rett patients exhibit a spectrum of  
537 disabilities. To establish an animal model of Rett that would incorporate the heterogeneity  
538 observed in patients, we used CRISPR to generate a mosaic knockdown of MeCP2 protein in  
539 *Xenopus laevis* tadpoles, which have been previously used to model neurodevelopmental  
540 diseases due to their evolutionary proximity to mammals and well-characterized neural  
541 development (Exner and Willsey, 2021; Pratt and Khakhalin, 2013).

542 Injection of *X. laevis* embryos at 4- or 8-cell stages using cas9 pre-complexed with  
543 sgRNA targeting 6 sites of the MeCP2 gene, including the regions corresponding to the DNA-  
544 binding domain, resulted in a tunable model of MeCP2 knockdown with a heterogeneous  
545 phenotype when assessed at the population level. Based on our target selection and injection  
546 strategy at the 4-cell stage, each individual animal was edited as a mosaic and presented  
547 varying degree of severity, without apparent toxicity from Cas9 or sgRNA. Indeed, all embryos  
548 developed to the swimming tadpole stages (Nieuwkoop-Faber stages 45-50) with no apparent  
549 loss of viability or morphological defect in earlier stages.

550 Importantly, swimming tadpoles with MeCP2 knock down (“Rett” tadpoles) exhibited a  
551 broad range of abnormal behavior compared to wild type vehicle-injected control tadpoles  
552 (“Control”) including darting motions and rapid repetitive swimming in tight circles (**Fig. 1a,b and**  
553 **Supplementary Movie 1**) reminiscent of the repetitive motions observed in human Rett patients  
554 as well as C-shaped or straight rigor (**Supplementary Movie 1**) that has been shown to

555 correspond to seizures in prior *Xenopus* studies (Hewapathirane et al., 2008). The cas9 protein  
556 and sgRNA doses were titrated to achieve between 5 and 95% gene editing efficiency as  
557 determined by qPCR without resulting in toxicity (**Supplementary Fig. 1a**). All tadpoles  
558 exhibited significant MeCP2 gene insertion/deletion polymorphisms (indels) at each of the  
559 mecp2 gene target sites (**Supplementary Fig. 1b**) and reduced MeCP2 RNA expression (**Fig.**  
560 **1c**). MeCP2 protein levels were also heterogeneously reduced in the brain (**Fig. 1d,e**) and  
561 olfactory multiciliated cells (MCC) (**Fig. 1d,f**). This editing approach resulted in an animal  
562 model of Rett with intra-subject and inter-subject diversity at molecular and phenotypic scales,  
563 which is similar to what is observed in humans.

564 In line with prior studies in humans and other model organisms (Sanfeliu et al., 2019, p.  
565 2), when we analyzed the transcriptome-wide effects of MeCP2 knockdown on the Rett  
566 phenotype in *Xenopus*, only subtle shifts in gene expression were detected with 70 out of  
567 10,935 genes probed undergoing a significant change in gene expression ( $p_{\text{adjusted}} < 0.05$ ) (**Fig.**  
568 **1g, Supplementary Table 1**). Of the 70 differentially expressed genes, 37 are involved in  
569 metabolic processes, 9 operate within developmental processes, and 8 are part of signal  
570 transduction pathways (**Supplementary Fig. 2a**); this aligns with changes in genes that control  
571 metabolism or regulate neuronal processes (e.g., ion transport, nervous system development) in  
572 Rett patients (Renthal et al., 2018).

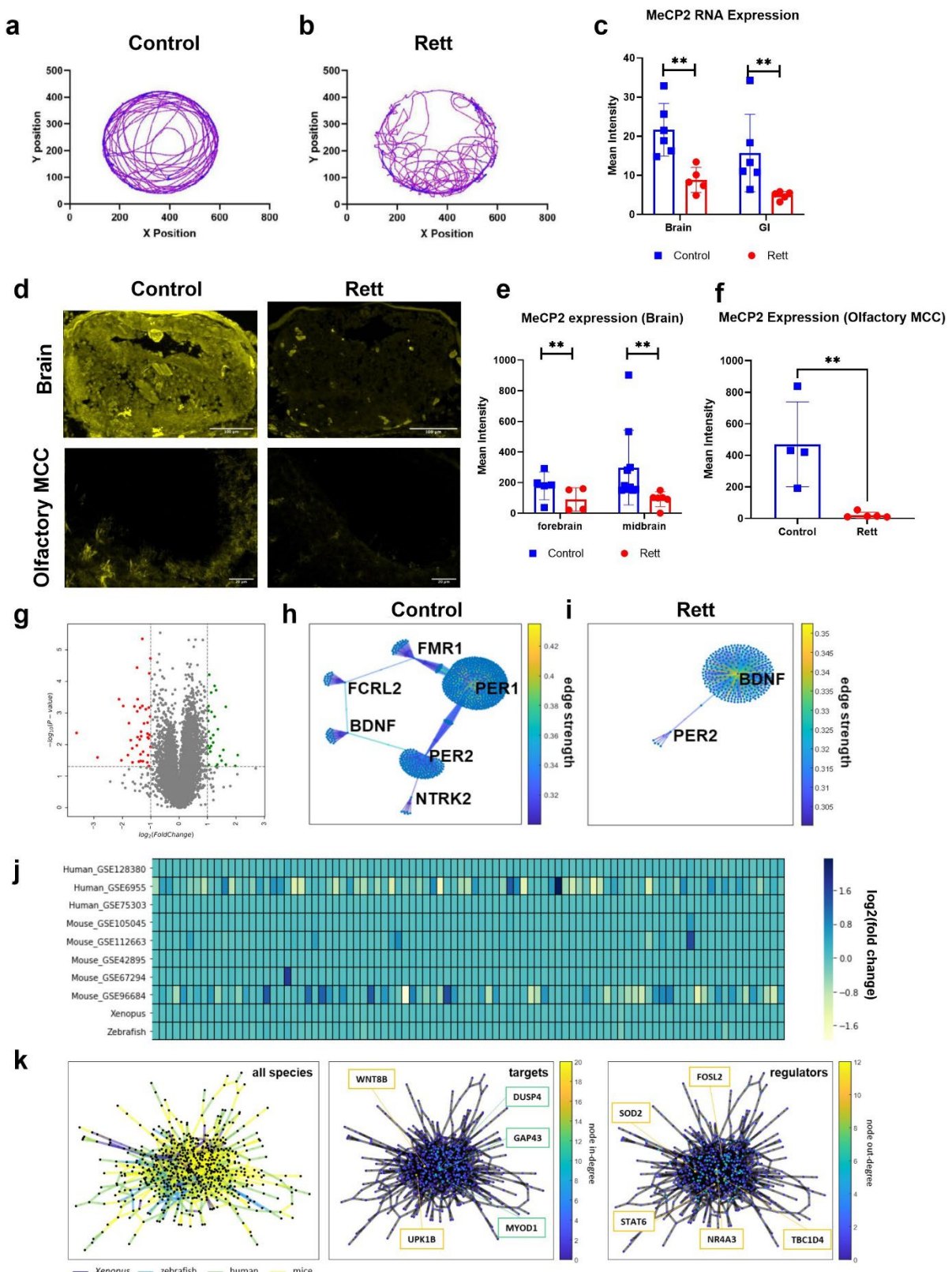
573 Interestingly, analysis of gene co-expression networks identified substantial  
574 reorganization from control animals (**Fig. 1h**) following MeCP2 knock down (**Fig. 1i**),  
575 characterized by a loss of strong connectivity among genes involved in the regulation of MeCP2  
576 (FMR1 and TRKB receptor NTRK2 (Abuhatzira et al., 2007; Arsenault et al., 2021)), neuronal  
577 development (BDNF (Chang et al., 2006; Li and Pozzo-Miller, 2014)),, and circadian rhythm  
578 (PER1, PER2 (Martínez de Paz et al., 2015)) all of which are altered in Rett patients (Li and  
579 Pozzo-Miller, 2014; Miller et al., 2019). Notably, after MeCP2 knock down, BDNF strengthened

580 as a network hub and exhibited greater co-expression connectivity amongst gene nodes (**Fig.**  
581 **1i**). This was unexpected because although BDNF is involved in neuronal development, synaptic  
582 transmission, and plasticity, it declines with the onset of Rett-like neuropathological and  
583 behavioral phenotypes (Li and Pozzo-Miller, 2014). However, BDNF is a known target of  
584 repression by MeCP2 and our findings are consistent with prior work suggesting that  
585 downregulation of BDNF is a later and indirect outcome of MeCP2 deficiency (Chang et al.,  
586 2006; Li and Pozzo-Miller, 2014).

587 We then comprehensively compared the effects of MeCP2 knock down in *Xenopus* to  
588 changes observed in published transcriptomic data sets from Rett patients as well as MeCP2  
589 knockout mouse and zebrafish models (**Supplementary Table 2**). After performing  
590 dimensionality reduction in this cross-species analysis, K-Means clustering applied to the  
591 principal components revealed 3 clusters, with mouse and human clustering together and  
592 zebrafish and *Xenopus* forming 2 independent clusters (**Supplementary Fig. 2b**). Importantly,  
593 diverse gene-expression abnormalities that occur across cell types in Rett syndrome could  
594 contribute to the differences observed across these datasets (Renthal et al., 2018). In this case,  
595 both the human and mouse transcriptomics were performed on brain tissues, whereas the  
596 zebrafish and *Xenopus* data are from whole organisms, which may account for the clustering  
597 patterns observed.

598 Despite evidence of species-specific clustering, a common gene signature comprised of  
599 96 genes was identified across all species by searching for genes with a fold change variance  
600 greater than mean variance. However, the common genes within this transcriptomic signature  
601 are expressed at similar low fold change levels in 7 of the 9 datasets analyzed, with slightly  
602 greater variations in expression only observed in 1 out of 5 mouse datasets and 1 out of 3  
603 human datasets (**Fig. 1j**). This finding provides additional evidence that mutation of MeCP2  
604 produces widespread, yet subtle, perturbations in gene expression.

605         Using gene co-expression network analysis (Huynh-Thu et al., 2010), we also identified  
606         interconnected gene sub-networks that are conserved across species and tissues in the MeCP2  
607         deficient condition (**Fig. 1k, Supplementary Tables 3 and 4**). Comparison across all species  
608         identified several shared major gene targets and regulators despite differences in species-  
609         specific network structure (**Supplementary Fig. 2c**). Interestingly, WNT8B, which is known to  
610         be modulated by the Rett-implicated gene Foxg1 (Aguiar et al., 2014), was found to be the most  
611         interconnected gene target within the MeCP2 cross-species network. The strongest gene  
612         regulators in this network, NR4A3 and SOD2, are both involved in oxidative metabolism, which  
613         is also known to be dysregulated in Rett Syndrome (De Felice et al., 2012). Thus, this CRISPR-  
614         enabled *Xenopus* model of Rett replicates many genetic and phenotypic features of the disease  
615         seen in humans.



617 **Figure 1: MeCP2 knockdown using CRISPR in *Xenopus laevis* tadpoles models Rett**  
618 **syndrome. a-b,** Tadpole models of Rett syndrome exhibit distinct swimming behavior in 60 mm  
619 diameter dishes following MeCP2 knockdown (“Rett”) compared to mock-injected controls  
620 (“Control”). MeCP2 RNA expression in brain and gastrointestinal (GI) tract using RNAscope, **c**,  
621 and protein in brain and multi-ciliated olfactory cells using immunohistochemistry, **d-f**, are  
622 significantly reduced in Rett syndrome tadpole models while maintaining a large degree of  
623 heterogeneity spatially, **d**, and across tissues, **e-f**; scale bars, 100  $\mu\text{m}$  in brain, 20  $\mu\text{m}$  in  
624 olfactory multi-ciliated cells. **g**, Volcano plot of differentially expressed genes showing that only  
625 70 genes are significantly up- or down-regulated following MeCP2 knockdown ( $p < 0.05$ , fold  
626 change  $>2$ , t-test with Bonferroni correction,  $N = 3$ ). Gene regulatory networks for control, **h**, and  
627 Rett, **i**, tadpoles reveal large network rearrangements with an increase in BDNF centrality. **j**,  
628 Comparison against other Rett syndrome models and clinical samples indicates minimal  
629 differential gene expression across the 96-gene signature developed to classify Rett syndrome.  
630 **k**, Network-level comparison across species and tissues (left) and identified shared target  
631 (middle) and regulator (right) genes.

632

### 633 **Computational discovery of drugs that reverse the network-level impact of Rett**

634 In Rett, MeCP2 knockout results in widespread but subtle gene expression patterns, and  
635 most effects are not detectable using standard statistical analysis. Researchers have applied  
636 network-based analytical methods to uncover previously-hidden connections within RNA and  
637 protein interaction networks (Miller et al., 2019; Sanfelix et al., 2019; Varderidou-Minasian et al.,  
638 2020), but these approaches have not been applied to Rett syndrome therapeutics discovery.  
639 To leverage transcriptomics analysis for drug discovery, we developed a computational  
640 framework we termed nemoCAD (network model for causality-aware discovery)(**Fig. 2a**) that  
641 compares transcriptomic signatures of disease versus healthy control subjects to predict

642 compounds from the Library of Integrated Network-Based Cellular Signatures (LINCS) database  
643 (“NIH LINCS Program,” n.d.), including FDA-approved drugs, which have a high likelihood to  
644 reverse the disease signature state back to a healthy state. Though signature-based tools have  
645 been previously developed to enable drug discovery (e.g., CMAP (Lamb et al., 2006), NicheNet  
646 (Browaeys et al., 2020), GPSnet (Cheng et al., 2019)), a major drawback is the impact of the  
647 expression of any single gene or protein on the resulting prediction. To be used effectively,  
648 these tools require well-matched disease datasets to the human cell line-based datasets  
649 present in LINCS, which may not be feasible for many diseases.

650 In contrast, we pursued an entirely different approach to transcriptomics signature  
651 analysis that is based on a Bayesian network encoding directed gene-gene and drug-gene  
652 interactions. By leveraging data in LINCS containing transcriptomics results following single  
653 gene knockout/knockdown and overexpression as well as addition of drug perturbagens in  
654 human cells, we calculated the probabilities of pairwise interactions among all of the genes and  
655 drugs in a human gene-gene and drug-gene interaction network whose structure was extracted  
656 from Comparative Toxicogenomics Database (CTD) (“The Comparative Toxicogenomics  
657 Database | CTD,” n.d.), KEGG (Kanehisa and Goto, 2000), and TRRUST (Han et al., 2018).  
658 Unlike signature based computational tools that take gene expression signatures at face value,  
659 this probabilistic approach offers greater abstraction while prioritizing for the network impact of  
660 perturbations, including those caused by disease or addition of drugs, and thereby reduces the  
661 impact of tissue-specific or species-specific transcriptomic biases as well as the influence of the  
662 expression of any individual gene.

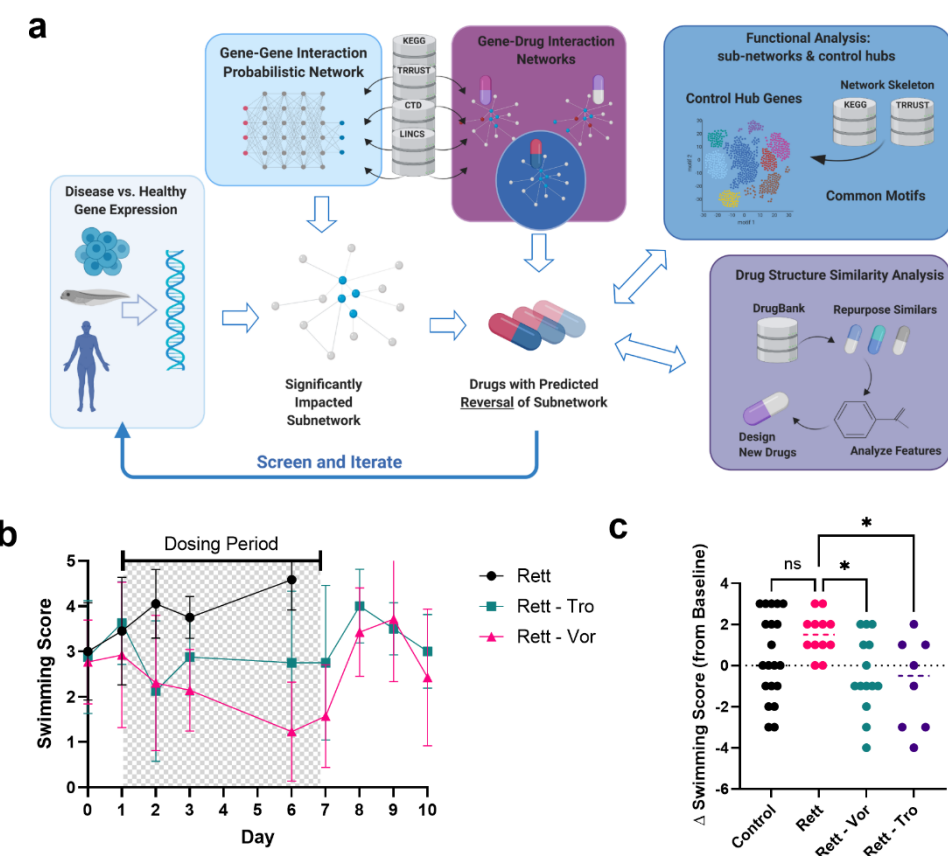
663 To identify drugs that might reverse disease states, we generated probabilistic network  
664 maps for each drug in the aggregate 19,800+ compound dataset. By inputting and comparing  
665 gene microarray data from MeCP2 knockdown tadpoles versus vehicle-injected controls, we  
666 identified sets of differentially expressed genes contained within the gene-gene interaction

network with a p-value < 0.05 and a log<sub>2</sub> fold change between 0.7 and 3.1 in 0.3-fold-change increments. For each fold-change, we generated a ranked list of compounds predicted to induce reversal of transcriptome-wide changes of: 1) single gene states using a cross-correlation score, 2) single gene states using a cross-entropy score, and 3) an overall gene network state score corresponding to the probability of involvement of the drug nodes in the identified subnetwork. These drug lists were combined to identify drugs that were ranked by being most consistently predicted to reverse the Rett transcriptome-wide changes and robust across the computational settings (**Supplementary Table 5**). Drugs were manually down-selected based on available toxicity data and to prioritize chemical diversity for initial screening. Rett tadpoles or controls were then dosed with lead compounds for 7 days via the culture medium beginning 1-2 days after the onset of symptoms and after collecting baseline swimming behavior data. Animal behaviors (swimming pattern abnormalities and seizure stages) were recorded every other day during drug exposure and washout phases, and the severity of seizure-like events was used as a screening metric.

These studies revealed that the FDA-approved drugs, vorinostat and ivermectin, demonstrated time-dependent reductions in seizure score that reversed after the drugs were washed out (**Fig. 2b; Supplementary Fig. 3**). However, we focused on vorinostat rather than ivermectin in all subsequent studies due to its higher predicted scoring consistency over time, more favorable reported pharmacokinetics, and its ability, albeit limited, to cross the blood-brain barrier. As a positive control with which to gauge relative efficacy, we also evaluated trofinetide, the synthetic IGF-1 C-terminal tripeptide. Although only moderately effective in recent Phase III Rett syndrome clinical trial top-line results that aligned with Phase II trial outcomes (Glaze et al., 2017), trofinetide represents the most relevant clinical-stage benchmark treatment. Importantly, in our Rett tadpole models, both trofinetide and vorinostat reduced seizure-like phenotypes and also increased viability (**Fig. 2b**). At day 6 of treatment, there was a statistically significant effect by both drugs on reducing swimming score relative to baseline before treatment onset (**Fig. 2c**).

693 As expected, no significant change was seen in WT and Rett vehicle-treated animals. This  
694 head-to-head comparison has supported the possibility that our *Xenopus* population-level model  
695 of Rett can offer predictive value for drug development.

696



697

698 **Figure 2: Network-based computational prediction of effective drugs to treat Rett**

699 **syndrome in tadpole models. a,** Network model for causality-aware discovery (nemoCAD)

700 combines a directed gene-gene and drug-gene interaction network extracted from CTD,

701 TRRUST, and KEGG databases with interaction probabilities inferred from single gene and drug

702 perturbations in LINCS. Transcriptome data from any disease model or patient and

703 corresponding control are used to identify the relevant subnetwork and disease-specific “node

704 weights” that account for probabilities of up-/down-regulation of a gene. A drug-gene interaction

705 probability matrix, inferred from LINCS, is computationally screened against the disease-specific

706 subnetwork to identify compounds that significantly interact with the subnetwork and are ranked

707 by their predicted ability to restore the disease transcriptome back to a healthy state based on

708 single gene and gene network signatures. Downstream analyses can be performed on the

709 resulting gene-gene interaction subnetwork by interrogating the underlying subnetwork structure  
710 to find control nodes and other network metrics. Additionally, the chemical structures of the  
711 predicted drugs can be clustered by structural similarity based on SMILES notation and  
712 annotated protein targets and pathways from DrugBank data. **b**, Graph showing relative effects  
713 on seizure score over 10 days of treatment in MeCP2 KD tadpoles of vehicle and 25 µM  
714 vorinostat (Rett - Vor) versus 70 µg/mL trofinetide (Rett - Tro), a clinical-stage drug with  
715 demonstrated efficacy (tadpoles per condition and timepoint: N = 12 Rett - Vor and Vehicle, N =  
716 8 Rett - Tro; error bars indicate s.d.; ANOVA P = 0.028 Vehicle-treated MeCP2 KD tadpoles did  
717 not survive past day 3 of the treatment period in one study and past day 6 in a second study. **c**,  
718 Change in swimming score at day 6 of treatment vs. baseline (day 0) is significantly improved  
719 by both drugs. \*, P < 0.05.

720

721

722 To understand the protein targets of both drugs, we adapted thermal proteome profiling  
723 (Franken et al., 2015; Huber et al., 2015; Mateus et al., 2017) that identifies molecules that  
724 drugs bind directly to protein targets for use with a whole exothermic animal (*Xenopus* tadpole)  
725 as well as using isolated body segments (head, viscera, tail). While we were able to detect  
726 some of the known histone deacetylase (HDAC) targets of vorinostat, we also found that both  
727 this drug and ivermectin bind to multiple other proteins related more broadly to acetylation  
728 metabolism, beyond histones and HDACs (**Supplementary Table 6**). These findings suggest a  
729 potential mechanism of action for the Rett normalizing responses we observed that involves  
730 restoration of normal acetyl-CoA metabolism and post-translational acetylation.

731 As these observations initially aligned with results of prior studies of HDAC6 acetylation  
732 of tubulin in cells of Rett patients (Gold et al., 2015; Lebrun et al., 2021) and microtubule  
733 modulation in closely-related CDKL5 deficiency disorder (Barbiero et al., 2019), we analyzed

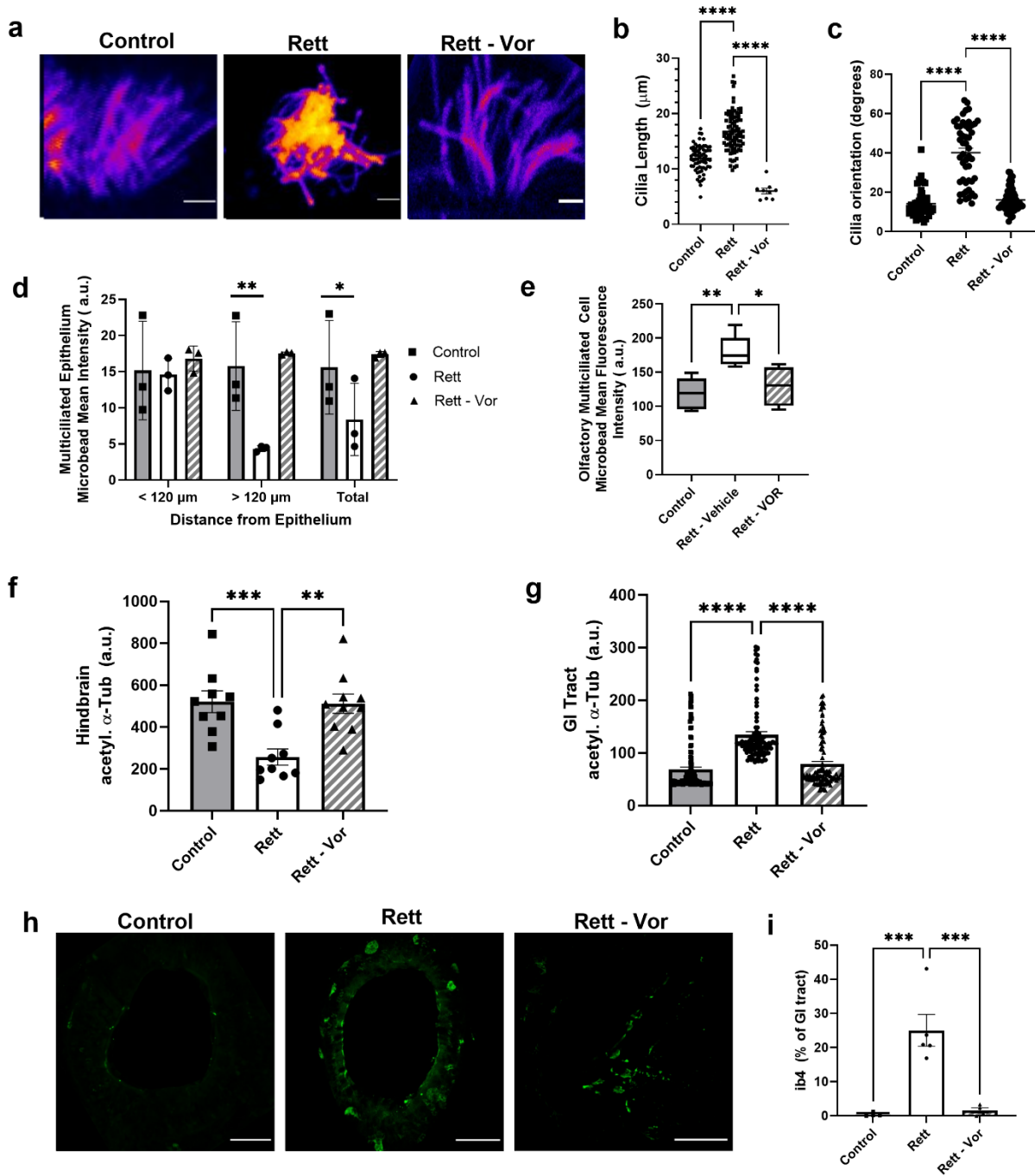
734 tadpole tissues for  $\alpha$ -tubulin acetylation and observed surprising bidirectional shifts in  
735 acetylation patterns depending on the tissue type. For example,  $\alpha$ -tubulin was hypoacetylated in  
736 neurons in sections of the midbrain (**Supplementary Fig. 4a**) and hindbrain (**Fig. 3f**) and  
737 increased in GI tract (**Fig. 3g**) and olfactory multi-ciliated cells (**Supplementary Fig. 4b**) and  
738 following MeCP2 knockdown, resulting in more sparse but dense tangles. Higher resolution  
739 imaging revealed that the cilia were longer and misaligned on multiciliated cells compared to  
740 controls (**Fig. 3a**), and both length (**Fig. 3b**) and orientation (**Fig. 3c**) were restored by  
741 vorinostat treatment.

742 We then evaluated the impact of ciliary morphology and organization on ciliary function  
743 using fluorescent microparticles (**Supplemental Fig. 5**). The disruption of ciliary beating-  
744 induced flow on the surface of skin (**Fig. 3d**) and olfactory multiciliated cells (**Fig. 3e**) due to  
745 MeCP2 knockdown is reversed by vorinostat treatment, suggesting that ciliary function  
746 restoration is linked to ciliary function.

747 Due to the prevalence of GI symptoms in Rett patients and our observation of tubulin  
748 acetylation disruption and vorinostat-induced recovery in the GI tract (**Fig. 3g**), we further  
749 explored the role of MeCP2 knockdown in the gut. Staining for isolectin B4-positive (ib4+) cells  
750 to assess GI tract inflammation and nociceptive innervation, which is increased in Rett patients  
751 (Baikie et al., 2014; Downs et al., 2010), revealed that tadpoles exhibited significant ib4+  
752 expression due to MeCP2 knockdown (**Fig. 3h,i**), which vorinostat again reversed.

753

754



755

756

757

758

759

760

761 **Figure 3: Vorinostat treatment of Rett tadpoles restores ciliary function, normalizes hypo-**  
762 **and hyperacetylated tubulin across tissues, and reduces GI tract inflammation. a,**  
763 Olfactory cell ciliary abnormalities due to MeCP2 knockdown were restored by treatment with  
764 vorinostat (magenta-yellow colormap of fluorescence intensity, cilia stained for tubulin),  
765 significantly restoring their **b**, length and **c**, orientation (\*\*\*\*, P < 0.0001). Functional rescue of  
766 cilia was also observed in both epithelial, **d**, and olfactory multiciliated cells in a microbead  
767 clearance assay (\*, P < 0.05; \*\*, P < 0.01). Despite the canonical HDACi activity of vorinostat,  
768 both hypoacetylated tubulin in the hindbrain, **f**, as well as hyperacetylated tubulin in the GI tract,  
769 **g**, was normalized. **h**, immunofluorescence images and **i**, plot showing that the % of ib4+ cells in  
770 the GI tract of tadpoles is increased in Rett tadpoles, which is indicative of inflammation and  
771 heightened pain response, and that this can be rescued by vorinostat treatment.

772

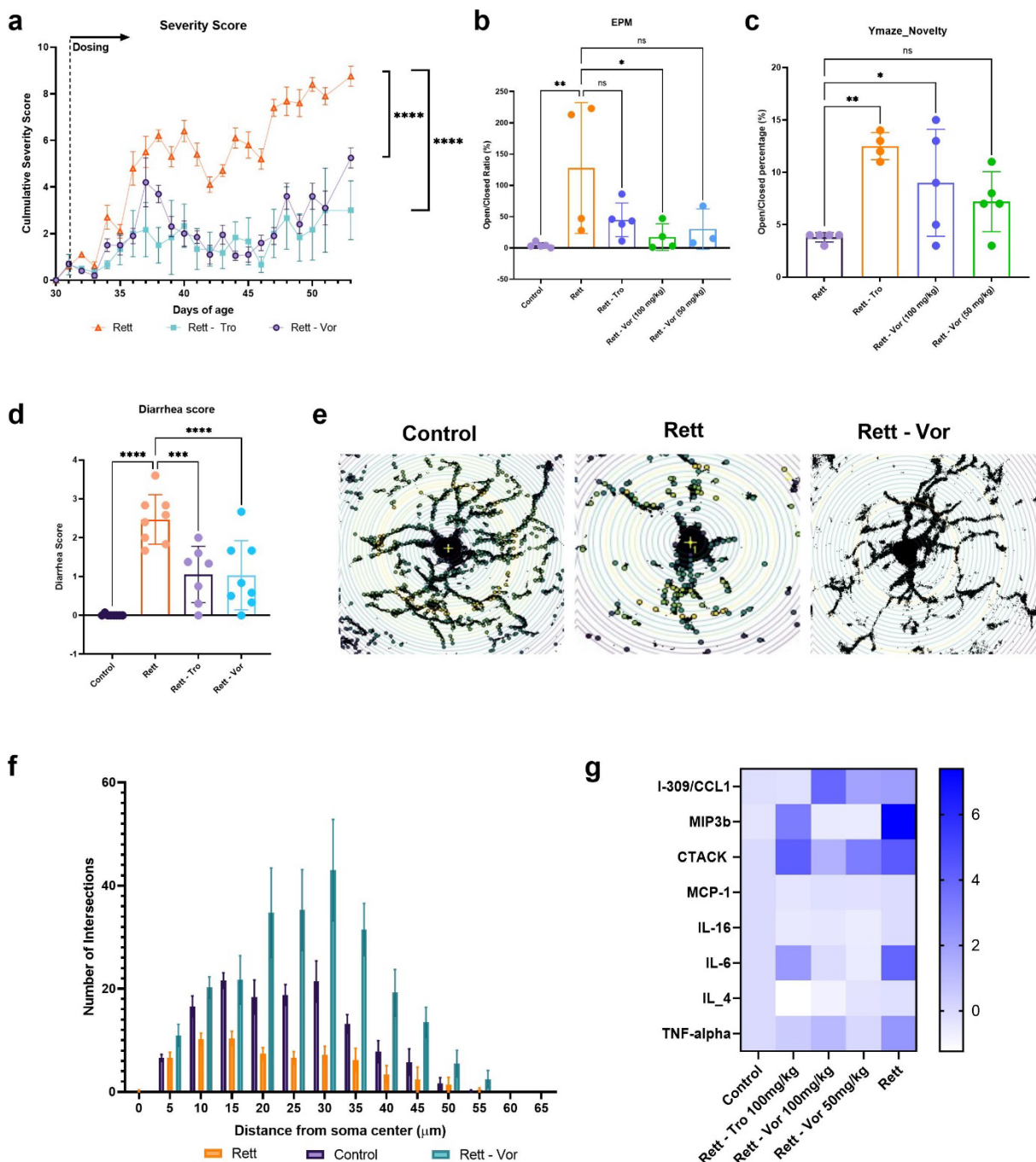
773 **Vorinostat normalizes the Rett phenotype in a mouse model**

774 Because vorinostat was predicted to reverse the Rett state in our computational studies,  
775 we evaluated its efficacy in the MeCP2-deficient male (*MeCP2<sup>-/-</sup>*) mouse Rett model that is  
776 commonly used in pre-clinical studies for Rett therapeutics, including trofinetide (Guy et al.,  
777 2001). We first treated younger animals starting at day 31 post-partum (p31) as was done in  
778 previous studies and confirmed that daily intraperitoneal (i.p.) administration of trofinetide (100  
779 mg/kg) results in significant amelioration of multiple disease-related parameters, including  
780 diarrhea and motor function, measured by a reduction in the established Bird score (Guy et al.,  
781 2007) that incorporates a broad range of Rett-related CNS and non-CNS symptoms. When  
782 vorinostat (50 mg/kg) and trofinetide were similarly administered i.p. on a daily basis over two  
783 weeks and compared with vehicle control, we found that animals responded favorably to both  
784 drugs (**Fig. 4a**); however, treatment with vorinostat resulted in improved neurological function  
785 compared to trofinetide, as determined by measuring elevated plus maze (EPM) performance

786 (Fig. 4b). Both drugs also resulted in enhanced spatial novelty Y-maze performance (Fig. 4c)  
787 and an improved diarrhea score (Fig. 4d).

788 As brain microglia have been implicated in Rett progression and therapeutic effects  
789 (Cronk et al., 2015; Derecki et al., 2012; Schafer et al., 2016) based on their role in  
790 neuroinflammation, waste removal, and synaptic pruning, we immuno-stained for microglia  
791 using ionized calcium binding adaptor molecule (Iba-1), a microglia-specific marker, in sections  
792 of MeCP2<sup>-/-</sup> mouse brains. Using Sholl analysis to assess microglia morphology (Timmerman et  
793 al., 2018), we found that the MeCP2<sup>-/-</sup> microglia exhibited significantly stunted morphology with  
794 fewer projection crossings compared to WT littermates, indicative of a heightened inflammatory  
795 state, which vorinostat restored (Fig. 4e,f). This result, together with the reduction of multiple  
796 serum inflammatory markers, including TNF- $\alpha$ , IL-4, IL-6, IL-16, CCL2, MIP3b, and CCI1 (Fig.  
797 4g), suggests that animals with Rett experience a heightened inflammatory state, and that  
798 treatment with vorinostat can suppress this inflammation.

799



800  
801  
802

803 **Figure 4: Vorinostat rescues multiple Rett syndrome-related CNS and somatic**  
804 **symptoms. a,** Bird severity scores measured in MeCP2<sup>-/-</sup> mice treated with vehicle (Rett),

805 trofinetide (100 mg/kg), or vorinostat (50 mg/kg) from day 31 to 51 of age (ANOVA; \*\*\*\*, P <  
806 0.0001). **b**, elevated-plus maze and, **c**, Y-novelty maze cognitive tests of MeCP2<sup>-/y</sup> mice  
807 comparing vorinostat treatment efficacy to vehicle and trofinetide (ANOVA and Holm-Šídák test;  
808 \*, P < 0.05; \*\*, P < 0.01). **d**, diarrhea scored using a 0-3 scale (ANOVA and Holm-Šídák test;  
809 \*\*\*, P < 0.001; \*\*\*\*, P < 0.0001). Representative images of Sholl analysis of microglial  
810 arborization in mouse olfactory (**e**) and the Sholl analysis graph showing the branching profile of  
811 microglia (**f**) in control versus Rett mice treated with or without vorinostat (ANOVA and Holm-  
812 Šídák test; Control vs. Rett, P = 0.0004; Control vs. Vor, P < 0.0001). **g**, Levels of indicated  
813 cytokines measured in plasma of control mice versus Rett mice with or without treatment with  
814 trofinetide (Rett – Tro, 100 mg/kg), vorinostat (Rett – Vor, 50 mg/kg), or vehicle (Rett) for 3  
815 weeks (mean values shown, N = 3, scale at right indicates z-score normalized to wild-type  
816 vehicle-treated littermates). The observed baseline inflammatory state in Rett mice agreed with  
817 published effects of MeCP2 knockdown(O'Driscoll et al., 2015).

818

### 819 **Oral vorinostat exhibits broad efficacy in Rett mice even after onset of symptoms**

820 Pre-clinical studies for Rett therapies routinely dose MeCP2<sup>-/y</sup> mice prior to the onset of  
821 symptoms (Castro et al., 2014; Szczesna et al., 2014) due to the rapid onset of symptoms and  
822 short lifespan of animals, in contrast to patients who seek clinical care due to developmental  
823 deficits which may not be diagnosed for several years before treatment could be initiated  
824 (Tarquinio et al., 2015). To better mimic this more relevant clinical scenario, male MeCP2<sup>-/y</sup>  
825 mice were dosed approximately one week after the onset of symptoms. Also, because long term  
826 treatment of Rett patients would be best served by oral administration, and due to the fact that  
827 our results showed a reduction in diarrhea in mice treated with vorinostat via daily i.p., we tested  
828 the efficacy of an oral formulation of vorinostat. Interestingly, when we administered trofinetide  
829 i.p. after symptoms developed in this model, it was found to be ineffective based on overall Rett  
830 score, similar to the moderate efficacy observed in human clinical trials, whereas oral vorinostat

831 (50 mg/kg) prevented significant worsening of the symptom severity score (**Fig. 5a**), ameliorated  
832 weight gain, and increased performance in EPM (**Fig. 5b**) and Y mazes (**Fig. 5c**). Animals  
833 treated with oral vorinostat showed complete survival after 3 weeks of treatment, which is  
834 comparable to what would be expected for vehicle-treated Rett animals for a study of this  
835 duration, whereas only ~ 60% of trofinetide-treated Rett animals survived (**Fig. 5d**). To our  
836 knowledge, this represents the first effective treatment of MeCP2<sup>-/-</sup> mice when treatment is  
837 initiated *after* the onset of symptoms.

838 Rett patients and mouse Rett models exhibit significant declines in fine motor and gait  
839 control as well as GI tract dysfunction(Hagberg, 2002; Motil et al., 2012). Importantly, the  
840 deficiencies in mobility, gait, and hindlimb clasping, as well as increased diarrhea we also  
841 observed in MeCP2<sup>-/-</sup> animals were again rescued by vorinostat treatment (**Fig. 5e,f**). Breathing  
842 also was significantly improved following vorinostat treatment compared to trofinetide and  
843 vehicle treatments (**Fig. 5g**). Given the putative effects of vorinostat on acetylation metabolism  
844 and post-translational modification of tubulin and its disruption of ciliary function identified in  
845 tadpoles, we also analyzed  $\alpha$ -tubulin acetylation in the multi-ciliated cells in mouse lung  
846 bronchioles, which revealed an overall increase of hyperacetylated  $\alpha$ -tubulin in MeCP2<sup>-/-</sup>  
847 animals that vorinostat again restored (**Fig. 5h**). In addition, we explored the potential link of  
848 tubulin acetylation with muscle function and found that vorinostat treatment can rescue the  
849 disrupted  $\alpha$ -tubulin acetylation observed in femoral muscle sections (**Fig. 5i**). Increased  
850 acetylation due to the loss of MeCP2 may play a role in muscle function as hyperacetylation has  
851 been shown to increase stiffness and resistance in striatal muscles *in vitro* (Coleman et al.,  
852 2021).

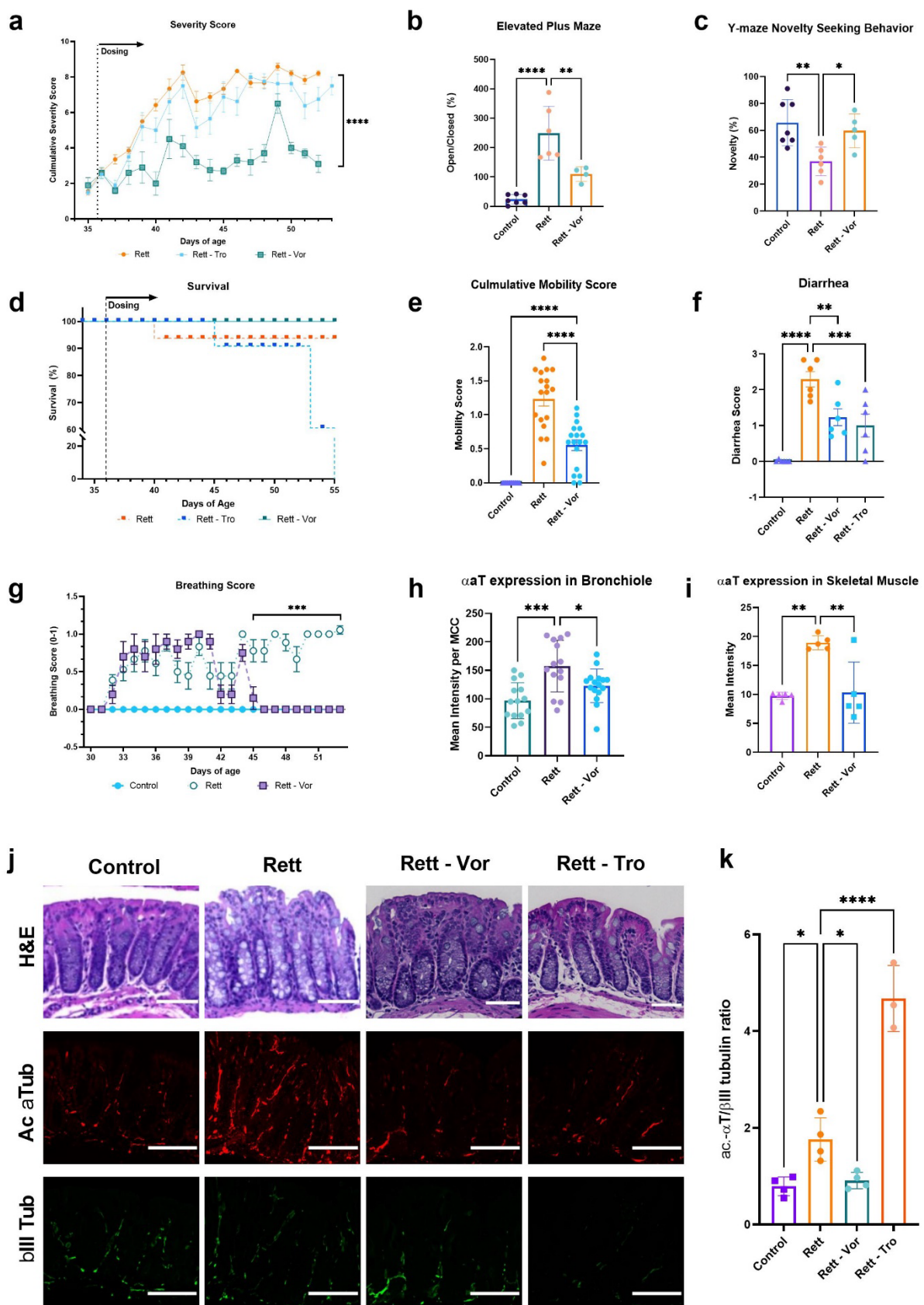
853 We continued to evaluate the possible impact of tubulin acetylation by examining the  
854 colon, a biomechanically-active organ that is often distended in Rett patients and may play a  
855 major role in digestive tract disruption that is a major complaint of these patients clinically (Motil

et al., 2012). Initial histological analysis of the colon indicated a greater degree of vacuolization and heightened neutrophil infiltrate in MeCP2-null animals, which vorinostat and trofinetide reversed (**Fig. 5j**). Staining of these sections for  $\beta$ III- and acetylated  $\alpha$ -tubulin also revealed that acetylated  $\alpha$ -tubulin is significantly more colocalized with neuronal staining in the colon in MeCP2-null mice, and that this can be normalized by treatment with either vorinostat or trofinetide (**Fig. 5j**). However, while vorinostat also normalized the ratio of acetylated  $\alpha$ -tubulin to  $\beta$ III-tubulin, it was unexpectedly worsened by trofinetide (**Fig. 5j,k**). While the developing GI tract of tadpoles prevented detailed analysis of their enteric neurons, the tubulin acetylation-normalizing effect of vorinostat identified by network analysis in *Xenopus* clearly translated to this mammalian (mouse) model at the cellular level.

These data show that oral dosing of vorinostat improved classical disease outcome metrics in MeCP2-null male mice and it ameliorated microglial dysfunction and hyperacetylation of tubulin in their GI and respiratory tracts as well as in skeletal muscle. Vorinostat also was recently shown to be effective in treating Fragile X syndrome (Ding et al., 2021), which is closely related to Rett, sharing both X-linked mutations and symptoms of autism, although it is caused by a mutation in the FMR1 gene. Interestingly, we identified a loss of gene network connectivity with FMR1 in the Rett-related *Xenopus* gene network (**Fig. 1h**), and genes with the maximum variation and fold change differences in humans with Fragile X also occurred in pathway classes involved in oxidative stress and multiple biosynthesis pathways that align with the major regulators we identified by the cross-species MeCP2 mutant network analysis (**Supplementary Figure 6a** and **Supplementary Tables 7 and 8**). Moreover, when we used nemoCAD to predict drugs that might reverse the Fragile X genotype in humans, both the compound classes and gene targets were similar to those predicted for *Xenopus* with MeCP2 knockdown, including a high number of PPAR receptor agonists, HDAC inhibitors, and cyclooxygenase inhibitors (**Supplementary Figure 6b,c**). Thus, these computational results suggest more broadly that

881 developmental therapeutics approaches for neurodevelopmental disorders with similar broad  
882 transcriptional effects may benefit from using this form of gene interaction network analysis to  
883 identify network-level signatures characteristic of specific diseases and to predict drugs that  
884 may reverse those changes.

885



887 **Figure 5: Oral administration of vorinostat in MeCP2<sup>-/y</sup> mice after the onset of Rett  
888 symptoms rescues CNS and somatic symptoms. a,** Bird severity scores measured in  
889 MeCP2<sup>-/y</sup> mice treated with vehicle (Rett), trofinetide (100 mg/kg i.p.), or oral vorinostat (50  
890 mg/kg) from day 36, after onset of symptoms, showing significant suppression of symptoms by  
891 vorinostat treatment while trofinetide's effects were indistinguishable from the vehicle control  
892 (ANOVA, \*\*\*\*, P < 0.0001). **b,** elevated-plus maze and, **c,** Y-novelty maze cognitive tests of  
893 MeCP2<sup>-/y</sup> mice comparing vorinostat treatment efficacy to vehicle and trofinetide (ANOVA and  
894 Dunnett's multiple comparison test; \*, P < 0.05; \*\*, P < 0.01; \*\*\*\*, P < 0.0001). **d,** survival curve  
895 of animals in this study. **e,** mobility scored using a 0-2 scale and **f,** diarrhea scored using a 0-3  
896 scale (ANOVA and Holm-Šídák test; \*\*, P < 0.01 \*\*\*, P < 0.001; \*\*\*\*, P < 0.0001). **g,** breathing  
897 difficulty evaluated using a 0-1 score (ANOVA and Dunnett's multiple comparison test; \*\*\*, P <  
898 0.001). Graphs showing levels of hyperacetylated  $\alpha$ -tubulin in cells of the multi-ciliated cells in  
899 the bronchiolar epithelium of the lung (**h**) and skeletal muscle (**i**) in mice treated as described in  
900 **a** (data are presented as mean  $\pm$  s.d.; \*, P < 0.05; \*\*, P < 0.01; \*\*\*, P < 0.001). **j,** Hematoxylin  
901 and eosin (H&E) stained histological sections of colon from the control and drug-treated mice  
902 (top row) and immunofluorescent staining for acetylated  $\alpha$ -tubulin (middle) and  $\beta$ III-tubulin  
903 (bottom) in these sections. **k,** Graph showing changes in the  $\beta$ III-tubulin ratio in drug-treated  
904 versus control colon tissues (\*, P < 0.05; \*\*\*\*, P < 0.0001).

905

## 906 **DISCUSSION**

907 Taken together, our results demonstrate the value of combining computational network  
908 analysis-based drug repurposing algorithms with CRISPR technology to rapidly build novel *in*  
909 *vivo* disease models using *X. laevis* that can be used to generate data and carry out screening  
910 of drugs with activities of interest predicted computationally. The *Xenopus* tadpole model  
911 developed here, which was generated in our laboratory within 3 weeks, exhibits a large degree

912 of genetic and phenotypic heterogeneity that reduces risks associated with computational and  
913 screening outcomes by better capturing the disease state. Importantly, the *Xenopus* results  
914 translated well to a mouse Rett model, and hence the tadpole model offers a faster, lower-cost,  
915 and potentially much higher throughput alternative to mammalian models. In addition, our  
916 target-agnostic computational approach enabled rapid discovery of novel mechanisms,  
917 including the counterintuitive ability of an HDAC inhibitor to normalize both hypoacetylated  
918 tubulin in the CNS and hyperacetylated tubulin in other organs, as well as identify drugs that  
919 have broad efficacy across multiple organs. This approach led to the first demonstration of  
920 efficacy in the mouse MeCP2 knockout model of Rett syndrome even when treated after the  
921 onset of symptoms, in contrast with the lack of efficacy of trofinetide. Given the modest efficacy  
922 of trofinetide in the clinic, conducting pre-clinical studies to restore health after the onset of  
923 symptoms as in our *Xenopus* screen may be a more robust benchmark for efficacy in complex  
924 CNS disorders. The drug discovery platform presented here offers Rett and other  
925 neurodevelopmental patients the possibility of single small molecule therapeutics that address  
926 multiple fundamental disease-modifying pathways with a broad clinical impact. Furthermore, by  
927 identifying and rapidly evaluating existing drugs, potentially even in patients, our platform  
928 enables the discovery of hidden therapeutic mechanisms for new drug development.  
929

### 930 **ACKNOWLEDGEMENTS**

931 We would like to thank Dr. Barbara J. Calderone for guidance and assistance with the  
932 mouse neurobehavioral assays, Dr. Amanda Graveline, Sarai Bardales, Andyna Vernet and  
933 Melissa Sanchez-Ventura for their assistance with mouse studies, Thomas C. Ferrante for  
934 guidance and assistance with image acquisition and analysis, Dr. Lay-Hong Ang and Suzanne  
935 White for tissue immunostaining support, Dr. Aurelien Begue and Mahmoud El-Rifai for their  
936 assistance with RNAscope experiments, and Erin Switzer and Emma Lederer for help with

937     *Xenopus* embryo fertilization and husbandry. All behavioral experiments were conducted at the  
938     HMS Mouse Behavioral Core facility. M.L. gratefully acknowledges support of the Elisabeth  
939     Giaque Trust, London. We are grateful for funding from the Wyss Institute for Biologically  
940     Inspired Engineering at Harvard University through Validation Project support.

941     **COMPETING INTERESTS**

942     RN, FV, EG, ML, and DEI hold equity in Unravel Biosciences, Inc.; RN, FV, and DEI are  
943     members of its board of directors; ML and DEI are members of its scientific advisory board; and  
944     RN, FV, and EG are current employees of the company.

945     **AUTHOR CONTRIBUTIONS**

946         RN, FV, and DEI conceived of and directed the work. RN, TL, MS, FV, EG, KS, KV, and  
947         AV conducted animal studies and in vitro analyses. FV, MS, and VK developed and performed  
948         CRISPR generation of Rett tadpole models with guidance by ML. SK, MS, SL, VC, and TT  
949         performed bioinformatic analysis and computational drug prediction. SL and RN designed and  
950         developed nemoCAD software. JRT guided GI tract and lung immunostaining studies and  
951         evaluated the histology and tissue staining. RN and DEI wrote the manuscript. All authors  
952         reviewed and provided input for the manuscript.

953     **DATA AVAILABILITY**

954         All data used in this study, including the *Xenopus* microarray data, are publicly available  
955         using accession codes listed in **Supplementary Table 2**.

956     **CODE AVAILABILITY**

957         Code is available upon reasonable request to the corresponding author.

958 **REFERENCES**

- 959 Abdala AP, Lioy DT, Garg SK, Knopp SJ, Paton JFR, Bissonnette JM. 2014. Effect of Sarizotan, a 5-HT<sub>1a</sub>  
960 and D<sub>2</sub>-Like Receptor Agonist, on Respiration in Three Mouse Models of Rett Syndrome. *Am J  
961 Respir Cell Mol Biol* **50**:1031–1039. doi:10.1165/rcmb.2013-0372OC
- 962 Abuhatzira L, Makedonski K, Kaufman Y, Razin A, Shemer R. 2007. MeCP2 Deficiency in the Brain  
963 Decreases BDNF Levels by REST/CoREST-Mediated Repression and Increases TRKB Production.  
964 *Epigenetics* **2**:214–222. doi:10.4161/epi.2.4.5212
- 965 Aguiar DP, Sghari S, Creuzet S. 2014. The facial neural crest controls fore- and midbrain patterning by  
966 regulating Foxg1 expression through Smad1 activity. *Development* **141**:2494–2505.  
967 doi:10.1242/dev.101790
- 968 Arsenault J, Hooper AWM, Gholizadeh S, Kong T, Pacey LK, Koxhioni E, Niibori Y, Eubanks JH, Wang L-Y,  
969 Hampson DR. 2021. Interregulation between fragile X mental retardation protein and methyl  
970 CpG binding protein 2 in the mouse posterior cerebral cortex. *Hum Mol Genet* **29**:3744–3756.  
971 doi:10.1093/hmg/ddaa226
- 972 Aslan Y, Tadjudide E, Zorn AM, Cha S-W. 2017. High-efficiency non-mosaic CRISPR-mediated knock-in and  
973 indel mutation in F0 Xenopus. *Development* **144**:2852–2858. doi:10.1242/dev.152967
- 974 Baikie G, Ravikumara M, Downs J, Naseem N, Wong K, Percy A, Lane J, Weiss B, Ellaway C, Bathgate K,  
975 Leonard H. 2014. Gastrointestinal dysmotility in Rett syndrome. *J Pediatr Gastroenterol Nutr*  
976 **58**:237–244. doi:10.1097/MPG.0000000000000200
- 977 Barbiero I, De Rosa R, Kilstrup-Nielsen C. 2019. Microtubules: A Key to Understand and Correct Neuronal  
978 Defects in CDKL5 Deficiency Disorder? *Int J Mol Sci* **20**:4075. doi:10.3390/ijms20174075
- 979 Basu T, O’Riordan KJ, Schoenike BA, Khan NN, Wallace EP, Rodriguez G, Maganti RK, Roopra A. 2019.  
980 Histone deacetylase inhibitors restore normal hippocampal synaptic plasticity and seizure

- 981 threshold in a mouse model of Tuberous Sclerosis Complex. *Sci Rep* **9**:5266.
- 982 doi:10.1038/s41598-019-41744-7
- 983 Browaeys R, Saelens W, Saeys Y. 2020. NicheNet: modeling intercellular communication by linking
- 984 ligands to target genes. *Nat Methods* **17**:159–162. doi:10.1038/s41592-019-0667-5
- 985 Carobrez AP, Bertoglio LJ. 2005. Ethological and temporal analyses of anxiety-like behavior: The elevated
- 986 plus-maze model 20 years on. *Neurosci Biobehav Rev, Defensive Behavior* **29**:1193–1205.
- 987 doi:10.1016/j.neubiorev.2005.04.017
- 988 Castro J, Garcia RI, Kwok S, Banerjee A, Petracic J, Woodson J, Mellios N, Tropea D, Sur M. 2014.
- 989 Functional recovery with recombinant human IGF1 treatment in a mouse model of Rett
- 990 Syndrome. *Proc Natl Acad Sci U S A* **111**:9941–9946. doi:10.1073/pnas.1311685111
- 991 Chahrour M, Zoghbi HY. 2007. The Story of Rett Syndrome: From Clinic to Neurobiology. *Neuron* **56**:422–
- 992 437. doi:10.1016/j.neuron.2007.10.001
- 993 Chang Q, Khare G, Dani V, Nelson S, Jaenisch R. 2006. The disease progression of MeCP2 mutant mice is
- 994 affected by the level of BDNF expression. *Neuron* **49**:341–348.
- 995 doi:10.1016/j.neuron.2005.12.027
- 996 Cheng F, Lu W, Liu C, Fang J, Hou Y, Handy DE, Wang R, Zhao Y, Yang Y, Huang J, Hill DE, Vidal M, Eng C,
- 997 Loscalzo J. 2019. A genome-wide positioning systems network algorithm for in silico drug
- 998 repurposing. *Nat Commun* **10**:1–14. doi:10.1038/s41467-019-10744-6
- 999 Chien Y-H, Srinivasan S, Keller R, Kintner C. 2018. Mechanical Strain Determines Cilia Length, Motility,
- 1000 and Planar Position in the Left-Right Organizer. *Dev Cell* **45**:316–330.e4.
- 1001 doi:10.1016/j.devcel.2018.04.007
- 1002 Coleman AK, Joca HC, Shi G, Lederer WJ, Ward CW. 2021. Tubulin acetylation increases cytoskeletal
- 1003 stiffness to regulate mechanotransduction in striated muscle. *J Gen Physiol* **153**:e202012743.
- 1004 doi:10.1085/jgp.202012743

- 1005 Collins AL, Levenson JM, Vilaythong AP, Richman R, Armstrong DL, Noebels JL, David Sweatt J, Zoghbi HY.
- 1006 2004. Mild overexpression of MeCP2 causes a progressive neurological disorder in mice. *Hum Mol Genet* **13**:2679–2689. doi:10.1093/hmg/ddh282
- 1007
- 1008 Colvin L, Fyfe S, Leonard S, Schiavello T, Ellaway C, Klerk N de, Christodoulou J, Msall M, Leonard H.
- 1009 2003. Describing the phenotype in Rett syndrome using a population database. *Arch Dis Child*
- 1010 **88**:38–43. doi:10.1136/adc.88.1.38
- 1011 Cronk JC, Derecki NC, Ji E, Xu Y, Lampano AE, Smirnov I, Baker W, Norris GT, Marin I, Coddington N, Wolf
- 1012 Y, Turner SD, Aderem A, Klibanov AL, Harris TH, Jung S, Litvak V, Kipnis J. 2015. Methyl-CpG
- 1013 Binding Protein 2 Regulates Microglia and Macrophage Gene Expression in Response to
- 1014 Inflammatory Stimuli. *Immunity* **42**:679–691. doi:10.1016/j.jimmuni.2015.03.013
- 1015 De Felice C, Signorini C, Leoncini S, Pecorelli A, Durand T, Valacchi G, Ciccoli L, Hayek J. 2012. The role of
- 1016 oxidative stress in Rett syndrome: an overview. *Ann N Y Acad Sci* **1259**:121–135.
- 1017 doi:10.1111/j.1749-6632.2012.06611.x
- 1018 Della F, Contarino A, Simon H, Koob GF, Gold LH. 2000. Genetic Differences in Response to Novelty and
- 1019 Spatial Memory Using a Two-Trial Recognition Task in Mice. *Neurobiol Learn Mem* **73**:31–48.
- 1020 doi:10.1006/nlme.1999.3919
- 1021 Derecki NC, Cronk JC, Lu Z, Xu E, Abbott SBG, Guyenet PG, Kipnis J. 2012. Wild-type microglia arrest
- 1022 pathology in a mouse model of Rett syndrome. *Nature* **484**:105–109. doi:10.1038/nature10907
- 1023 Ding Q, Wu X, Li X, Wang H. 2021. Vorinostat Corrects Cognitive and Non-Cognitive Symptoms in a
- 1024 Mouse Model of Fragile X Syndrome. *Int J Neuropsychopharmacol* pyab081.
- 1025 doi:10.1093/ijnp/pyab081
- 1026 Downs J, Géranton SM, Bebbington A, Jacoby P, Bahi-Buisson N, Ravine D, Leonard H. 2010. Linking
- 1027 MECP2 and pain sensitivity: The example of Rett syndrome. *Am J Med Genet A* **152A**:1197–1205.
- 1028 doi:10.1002/ajmg.a.33314

- 1029 Exner CRT, Willsey HR. 2021. Xenopus leads the way: Frogs as a pioneering model to understand the  
1030 human brain. *genesis* **59**:e23405. doi:10.1002/dvg.23405
- 1031 Forbes M. 2021. py-factorgraph.
- 1032 Franken H, Mathieson T, Childs D, Sweetman GMA, Werner T, Tögel I, Doce C, Gade S, Bantscheff M,  
1033 Drewes G, Reinhard FBM, Huber W, Savitski MM. 2015. Thermal proteome profiling for  
1034 unbiased identification of direct and indirect drug targets using multiplexed quantitative mass  
1035 spectrometry. *Nat Protoc* **10**:1567–1593. doi:10.1038/nprot.2015.101
- 1036 Gabel HW, Kinde B, Stroud H, Gilbert CS, Harmin DA, Kastan NR, Hemberg M, Ebert DH, Greenberg ME.  
1037 2015. Disruption of DNA-methylation-dependent long gene repression in Rett syndrome. *Nature*  
1038 **522**:89–93. doi:10.1038/nature14319
- 1039 Gaetani M, Sabatier P, Saei AA, Beusch CM, Yang Z, Lundström SL, Zubarev RA. 2019. Proteome Integral  
1040 Solubility Alteration: A High-Throughput Proteomics Assay for Target Deconvolution. *J Proteome*  
1041 *Res* **18**:4027–4037. doi:10.1021/acs.jproteome.9b00500
- 1042 Giacometti E, Luikenhuis S, Beard C, Jaenisch R. 2007. Partial rescue of MeCP2 deficiency by postnatal  
1043 activation of MeCP2. *Proc Natl Acad Sci* **104**:1931–1936. doi:10.1073/pnas.0610593104
- 1044 Glaze DG, Neul JL, Percy A, Feyma T, Beisang A, Yaroshinsky A, Stoms G, Zuchero D, Horrigan J, Glass L,  
1045 Jones NE. 2017. A Double-Blind, Randomized, Placebo-Controlled Clinical Study of Trofinetide in  
1046 the Treatment of Rett Syndrome. *Pediatr Neurol* **76**:37–46.  
1047 doi:10.1016/j.pediatrneurol.2017.07.002
- 1048 Gold WA, Lacina TA, Cantrill LC, Christodoulou J. 2015. MeCP2 deficiency is associated with reduced  
1049 levels of tubulin acetylation and can be restored using HDAC6 inhibitors. *J Mol Med Berl Ger*  
1050 **93**:63–72. doi:10.1007/s00109-014-1202-x
- 1051 Guy J, Gan J, Selfridge J, Cobb S, Bird A. 2007. Reversal of Neurological Defects in a Mouse Model of Rett  
1052 Syndrome. *Science* **315**:1143–1147. doi:10.1126/science.1138389

- 1053 Guy J, Hendrich B, Holmes M, Martin JE, Bird A. 2001. A mouse *Mecp2*-null mutation causes neurological  
1054 symptoms that mimic Rett syndrome. *Nat Genet* **27**:322–326. doi:10.1038/85899
- 1055 Hagberg B. 2002. Clinical manifestations and stages of rett syndrome. *Ment Retard Dev Disabil Res Rev*  
1056 **8**:61–65. doi:10.1002/mrdd.10020
- 1057 Han H, Cho J-W, Lee Sangyoung, Yun A, Kim H, Bae D, Yang S, Kim CY, Lee M, Kim E, Lee Sungho, Kang B,  
1058 Jeong D, Kim Y, Jeon H-N, Jung H, Nam S, Chung M, Kim J-H, Lee I. 2018. TRRUST v2: an  
1059 expanded reference database of human and mouse transcriptional regulatory interactions.  
1060 *Nucleic Acids Res* **46**:D380–D386. doi:10.1093/nar/gkx1013
- 1061 Hewapathirane DS, Dunfield D, Yen W, Chen S, Haas K. 2008. In vivo imaging of seizure activity in a novel  
1062 developmental seizure model. *Exp Neurol* **211**:480–488. doi:10.1016/j.expneurol.2008.02.012
- 1063 Hockly E, Richon VM, Woodman B, Smith DL, Zhou X, Rosa E, Sathasivam K, Ghazi-Noori S, Mahal A,  
1064 Lowden PAS, Steffan JS, Marsh JL, Thompson LM, Lewis CM, Marks PA, Bates GP. 2003.  
1065 Suberoylanilide hydroxamic acid, a histone deacetylase inhibitor, ameliorates motor deficits in a  
1066 mouse model of Huntington’s disease. *Proc Natl Acad Sci U S A* **100**:2041–2046.  
1067 doi:10.1073/pnas.0437870100
- 1068 Huber KVM, Olek KM, Müller AC, Tan CSH, Bennett KL, Colinge J, Superti-Furga G. 2015. Proteome-wide  
1069 drug and metabolite interaction mapping by thermal-stability profiling. *Nat Methods* **12**:1055–  
1070 1057. doi:10.1038/nmeth.3590
- 1071 Huynh-Thu VA, Irrthum A, Wehenkel L, Geurts P. 2010. Inferring Regulatory Networks from Expression  
1072 Data Using Tree-Based Methods. *PLOS ONE* **5**:e12776. doi:10.1371/journal.pone.0012776
- 1073 Kanehisa M, Goto S. 2000. KEGG: kyoto encyclopedia of genes and genomes. *Nucleic Acids Res* **28**:27–  
1074 30.
- 1075 Kerr AM, Nomura Y, Armstrong D, Anvret M, Belichenko PV, Budden S, Cass H, Christodoulou J, Clarke A,  
1076 Ellaway C, d’Esposito M, Francke U, Hulten M, Julu P, Leonard H, Naidu S, Schanen C, Webb T,

- 1077 Engerstrom IW, Yamashita Y, Segawa M. 2001. Guidelines for reporting clinical features in cases  
1078 with MECP2 mutations. *Brain Dev* **23**:208–211. doi:10.1016/S0387-7604(01)00193-0
- 1079 Kulkarni SS, Griffin JN, Date PP, Liem KF, Khokha MK. 2018. WDR5 Stabilizes Actin Architecture to  
1080 Promote Multiciliated Cell Formation. *Dev Cell* **46**:595-610.e3. doi:10.1016/j.devcel.2018.08.009
- 1081 Labun K, Montague TG, Gagnon JA, Thyme SB, Valen E. 2016. CHOPCHOP v2: a web tool for the next  
1082 generation of CRISPR genome engineering. *Nucleic Acids Res* **44**:W272-276.  
1083 doi:10.1093/nar/gkw398
- 1084 Lamb J, Crawford ED, Peck D, Modell JW, Blat IC, Wrobel MJ, Lerner J, Brunet J-P, Subramanian A, Ross  
1085 KN, Reich M, Hieronymus H, Wei G, Armstrong SA, Haggarty SJ, Clemons PA, Wei R, Carr SA,  
1086 Lander ES, Golub TR. 2006. The Connectivity Map: using gene-expression signatures to connect  
1087 small molecules, genes, and disease. *Science* **313**:1929–1935. doi:10.1126/science.1132939
- 1088 Lebrun N, Delépine C, Selloum M, Meziane H, Nectoux J, Herault Y, Bienvenu T. 2021. HDAC inhibitor  
1089 ameliorates behavioral deficits in Mecp2<sup>308/y</sup> mouse model of Rett syndrome. *Brain Res*  
1090 147670. doi:10.1016/j.brainres.2021.147670
- 1091 Li W, Pozzo-Miller L. 2014. BDNF deregulation in Rett syndrome. *Neuropharmacology*, BDNF Regulation  
1092 of Synaptic Structure, Function, and Plasticity **76**:737–746.  
1093 doi:10.1016/j.neuropharm.2013.03.024
- 1094 Lonowski LA, Narimatsu Y, Riaz A, Delay CE, Yang Z, Niola F, Duda K, Ober EA, Clausen H, Wandall HH,  
1095 Hansen SH, Bennett EP, Frödin M. 2017. Genome editing using FACS enrichment of nuclease-  
1096 expressing cells and indel detection by amplicon analysis. *Nat Protoc* **12**:581–603.  
1097 doi:10.1038/nprot.2016.165
- 1098 Luikenhuis S, Giacometti E, Beard CF, Jaenisch R. 2004. Expression of MeCP2 in postmitotic neurons  
1099 rescues Rett syndrome in mice. *Proc Natl Acad Sci U S A* **101**:6033–6038.  
1100 doi:10.1073/pnas.0401626101

- 1101 Martínez de Paz A, Sanchez-Mut JV, Samitier-Martí M, Petazzi P, Sáez M, Szczesna K, Huertas D, Esteller  
1102 M, Ausió J. 2015. Circadian Cycle-Dependent MeCP2 and Brain Chromatin Changes. *PLoS ONE*  
1103 **10**. doi:10.1371/journal.pone.0123693
- 1104 Mateus A, Määttä TA, Savitski MM. 2017. Thermal proteome profiling: unbiased assessment of protein  
1105 state through heat-induced stability changes. *Proteome Sci* **15**:13. doi:10.1186/s12953-017-  
1106 0122-4
- 1107 Miller RA, Ehrhart F, Eijssen LMT, Slenter DN, Curfs LMG, Evelo CT, Willighagen EL, Kutmon M. 2019.  
1108 Beyond Pathway Analysis: Identification of Active Subnetworks in Rett Syndrome. *Front Genet*  
1109 **10**:59. doi:10.3389/fgene.2019.00059
- 1110 Morton J, Snider TA. 2017. Guidelines for collection and processing of lungs from aged mice for  
1111 histological studies. *Pathobiol Aging Age-Relat Dis* **7**:1313676.  
1112 doi:10.1080/20010001.2017.1313676
- 1113 Motil KJ, Caeg E, Barrish JO, Geerts S, Lane JB, Percy AK, Annese F, McNair L, Skinner SA, Lee H-S, Neul JL,  
1114 Glaze DG. 2012. Gastrointestinal and nutritional problems occur frequently throughout life in  
1115 girls and women with Rett syndrome. *J Pediatr Gastroenterol Nutr* **55**:292–298.  
1116 doi:10.1097/MPG.0b013e31824b6159
- 1117 Nalle SC, Zuo L, Ong MLM, Singh G, Worthy lake AM, Choi W, Manresa MC, Southworth AP, Edelblum  
1118 KL, Baker GJ, Joseph NE, Savage PA, Turner JR. 2019. Graft-versus-host disease propagation  
1119 depends on increased intestinal epithelial tight junction permeability. *J Clin Invest* **129**:902–914.  
1120 doi:10.1172/JCI98554
- 1121 Nenni MJ, Fisher ME, James-Zorn C, Pells TJ, Ponferrada V, Chu S, Fortriede JD, Burns KA, Wang Y, Lotay  
1122 VS, Wang DZ, Segerdell E, Chaturvedi P, Karimi K, Vize PD, Zorn AM. 2019. Xenbase: Facilitating  
1123 the Use of Xenopus to Model Human Disease. *Front Physiol* **10**. doi:10.3389/fphys.2019.00154
- 1124 NIH LINCS Program. n.d. <https://lincsproject.org/>

- 1125 O'Driscoll CM, Lima MP, Kaufmann WE, Bressler JP. 2015. Methyl CpG binding protein 2 deficiency  
1126 enhances expression of inflammatory cytokines by sustaining NF- $\kappa$ B signaling in myeloid derived  
1127 cells. *J Neuroimmunol* **283**:23–29. doi:10.1016/j.jneuroim.2015.04.005
- 1128 Pearl J. 1982. Reverend bayes on inference engines: a distributed hierarchical approachProceedings of  
1129 the Second AAAI Conference on Artificial Intelligence, AAAI'82. Pittsburgh, Pennsylvania: AAAI  
1130 Press. pp. 133–136.
- 1131 Potts EM, Coppotelli G, Ross JM. 2020. Histological-Based Stainings using Free-Floating Tissue Sections. *J  
1132 Vis Exp JoVE*. doi:10.3791/61622
- 1133 Pratt KG, Khakhalin AS. 2013. Modeling human neurodevelopmental disorders in the *Xenopus* tadpole:  
1134 from mechanisms to therapeutic targets. *Dis Model Mech* **6**:1057–1065.  
1135 doi:10.1242/dmm.012138
- 1136 Przanowski P, Wasko U, Zheng Z, Yu J, Sherman R, Zhu LJ, McConnell MJ, Tushir-Singh J, Green MR,  
1137 Bhatnagar S. 2018. Pharmacological reactivation of inactive X-linked *Mecp2* in cerebral cortical  
1138 neurons of living mice. *Proc Natl Acad Sci* **115**:7991–7996. doi:10.1073/pnas.1803792115
- 1139 Renthal W, Boxer LD, Hrvatin S, Li E, Silberfeld A, Nagy MA, Griffith EC, Vierbuchen T, Greenberg ME.  
1140 2018. Characterization of human mosaic Rett syndrome brain tissue by single-nucleus RNA  
1141 sequencing. *Nat Neurosci* **21**:1670–1679. doi:10.1038/s41593-018-0270-6
- 1142 Russo PST, Ferreira GR, Cardozo LE, Bürger MC, Arias-Carrasco R, Maruyama SR, Hirata TDC, Lima DS,  
1143 Passos FM, Fukutani KF, Lever M, Silva JS, Maracaja-Coutinho V, Nakaya HI. 2018. CEMiTool: a  
1144 Bioconductor package for performing comprehensive modular co-expression analyses. *BMC  
1145 Bioinformatics* **19**:56. doi:10.1186/s12859-018-2053-1
- 1146 Ruthsatz K, Dausmann KH, Peck MA, Drees C, Sabatino NM, Becker LI, Reese J, Hartmann L, Glos J. 2018.  
1147 Thyroid hormone levels and temperature during development alter thermal tolerance and  
1148 energetics of *Xenopus laevis* larvae. *Conserv Physiol* **6**. doi:10.1093/conphys/coy059

- 1149 Sanfeliu A, Hokamp K, Gill M, Tropea D. 2019. Transcriptomic Analysis of MeCP2 Mutant Mice Reveals  
1150 Differentially Expressed Genes and Altered Mechanisms in Both Blood and Brain. *Front  
1151 Psychiatry* **10**:278. doi:10.3389/fpsyg.2019.00278
- 1152 Schafer DP, Heller CT, Gunner G, Heller M, Gordon C, Hammond T, Wolf Y, Jung S, Stevens B. 2016.  
1153 Microglia contribute to circuit defects in MeCP2 null mice independent of microglia-specific loss  
1154 of MeCP2 expression. *eLife* **5**:e15224. doi:10.7554/eLife.15224
- 1155 Sekhon RS, Briskine R, Hirsch CN, Myers CL, Springer NM, Buell CR, de Leon N, Kaepller SM. 2013. Maize  
1156 gene atlas developed by RNA sequencing and comparative evaluation of transcriptomes based  
1157 on RNA sequencing and microarrays. *PLoS One* **8**:e61005. doi:10.1371/journal.pone.0061005
- 1158 Subramanian A, Narayan R, Corsello SM, Peck DD, Natoli TE, Lu X, Gould J, Davis JF, Tubelli AA, Asiedu JK,  
1159 Lahr DL, Hirschman JE, Liu Z, Donahue M, Julian B, Khan M, Wadden D, Smith IC, Lam D, Liberzon  
1160 A, Toder C, Bagul M, Orzechowski M, Enache OM, Piccioni F, Johnson SA, Lyons NJ, Berger AH,  
1161 Shamji AF, Brooks AN, Vrcic A, Flynn C, Rosains J, Takeda DY, Hu R, Davison D, Lamb J, Ardlie K,  
1162 Hogstrom L, Greenside P, Gray NS, Clemons PA, Silver S, Wu Xiaoyun, Zhao W-N, Read-Button  
1163 W, Wu Xiaohua, Haggarty SJ, Ronco LV, Boehm JS, Schreiber SL, Doench JG, Bittker JA, Root DE,  
1164 Wong B, Golub TR. 2017. A Next Generation Connectivity Map: L1000 Platform and the First  
1165 1,000,000 Profiles. *Cell* **171**:1437-1452.e17. doi:10.1016/j.cell.2017.10.049
- 1166 Szczesna K, de la Caridad O, Petazzi P, Soler M, Roa L, Saez MA, Fourcade S, Pujol A, Artuch-Iribarri R,  
1167 Molero-Luis M, Vidal A, Huertas D, Esteller M. 2014. Improvement of the Rett Syndrome  
1168 Phenotype in a MeCP2 Mouse Model Upon Treatment with Levodopa and a Dopa-Decarboxylase  
1169 Inhibitor. *Neuropsychopharmacology* **39**:2846–2856. doi:10.1038/npp.2014.136
- 1170 Tarquinio DC, Hou W, Neul JL, Lane JB, Barnes KV, O'Leary HM, Bruck NM, Kaufmann WE, Motil KJ, Glaze  
1171 DG, Skinner SA, Annese F, Baggett L, Barrish JO, Geerts SP, Percy AK. 2015. Age of diagnosis in

- 1172 Rett syndrome: patterns of recognition among diagnosticians and risk factors for late diagnosis.
- 1173 *Pediatr Neurol* **52**:585-591.e2. doi:10.1016/j.pediatrneurol.2015.02.007
- 1174 The Comparative Toxicogenomics Database | CTD. n.d. <http://ctdbase.org/>
- 1175 Timmerman R, Burm SM, Bajramovic JJ. 2018. An Overview of in vitro Methods to Study Microglia. *Front Cell Neurosci* **12**. doi:10.3389/fncel.2018.00242
- 1177 Tsai P-Y, Zhang B, He W-Q, Zha J-M, Odenwald MA, Singh G, Tamura A, Shen L, Sailer A, Yeruva S, Kuo W-
- 1178 T, Fu Y-X, Tsukita S, Turner JR. 2017. IL-22 Upregulates Epithelial Claudin-2 to Drive Diarrhea and
- 1179 Enteric Pathogen Clearance. *Cell Host Microbe* **21**:671-681.e4. doi:10.1016/j.chom.2017.05.009
- 1180 Varderidou-Minasian S, Hinz L, Hagemans D, Posthuma D, Altelaar M, Heine VM. 2020. Quantitative
- 1181 proteomic analysis of Rett iPSC-derived neuronal progenitors. *Mol Autism* **11**:38.
- 1182 doi:10.1186/s13229-020-00344-3
- 1183 Vashi N, Justice MJ. 2019. Treating Rett syndrome: from mouse models to human therapies. *Mamm Genome*. doi:10.1007/s00335-019-09793-5
- 1185 Willsey HR. 2021. Whole-Mount RNA In Situ Hybridization and Immunofluorescence of Xenopus
- 1186 Embryos and Tadpoles. *Cold Spring Harb Protoc* **2021**:pdb.prot105635.
- 1187 doi:10.1101/pdb.prot105635
- 1188 Yang Z, Steentoft C, Hauge C, Hansen L, Thomsen AL, Niola F, Vester-Christensen MB, Frödin M, Clausen
- 1189 H, Wandall HH, Bennett EP. 2015. Fast and sensitive detection of indels induced by precise gene
- 1190 targeting. *Nucleic Acids Res* **43**:e59. doi:10.1093/nar/gkv126
- 1191